3

Atomic/Molecular-Level Simulations of Laser–Materials Interactions

Leonid V. Zhigilei, Zhibin Lin, Dmitriy S. Ivanov, Elodie Leveugle, William H. Duff, Derek Thomas, Carlos Sevilla, and Stephen J. Guy

Summary. Molecular/atomic-level computer modeling of laser–materials interactions is playing an increasingly important role in the investigation of complex and highly nonequilibrium processes involved in short-pulse laser processing and surface modification. This chapter provides an overview of recent progress in the development of computational methods for simulation of laser interactions with organic materials and metals. The capabilities, advantages, and limitations of the molecular dynamics simulation technique are discussed and illustrated by representative examples. The results obtained in the investigations of the laser-induced generation and accumulation of crystal defects, mechanisms of laser melting, photomechanical effects and spallation, as well as phase explosion and massive material removal from the target (ablation) are outlined and related to the irradiation conditions and properties of the target material. The implications of the computational predictions for practical applications, as well as for the theoretical description of the laser-induced processes are discussed.

3.1 Introduction

Short-pulse lasers are used in a diverse range of applications, from advanced materials processing, cutting, drilling, and surface micro- and nanostructuring [1,2] to pulsed-laser deposition of thin films and coatings [3], laser surgery [4, 5], and artwork restoration [6, 7], and to the exploration of the conditions for inertial confinement fusion, with the world's most energetic laser system being built at the National Ignition Facility at Lawrence Livermore National Laboratory [8]. At the fundamental science level, short-pulse laser irradiation has the ability to bring material into a highly nonequilibrium state and provides a unique opportunity to probe the material behavior under extreme conditions. In particular, optical pump-probe experiments have been used to investigate transient changes in the electronic structure of the irradiated surface with high (often subpicosecond) temporal resolution [9–13], whereas recent advances in time-resolved X-ray and electron diffraction

techniques [14–22] provide an opportunity to directly probe the ultrafast atomic dynamics in laser-induced structural transformations. Further optimization of experimental parameters in current applications, the emergence of new techniques, and interpretation of the results of probing the transient atomic dynamics in materials and at surfaces can be facilitated by computational modeling of laser–materials interactions.

One of the main challenges in the computational description of short-pulse laser interactions with materials is presented by the complex multiscale character of the cascade of interrelated processes triggered by the laser excitation. These processes, schematically illustrated in Fig. 3.1, include laser excitation of optically active states in the target material (electronic or vibrational, linear or nonlinear/multiphoton), relaxation/thermalization of the absorbed laser energy (electron–phonon energy transfer, intramolecular and intermolecular vibrational equilibration, nonthermal atomic dynamics), active structural and phase transformations occurring in the high-temperature/high-pressure region of the laser energy deposition (melting/denaturation/charring, generation of crystal defects, fracture/spallation, explosive boiling, and surface vaporization), as well as long-term evolution of multicomponent ablation plume (evaporation/condensation of clusters, chemical and ionization reactions). Computer modeling of this diverse range of processes is challenging and requires a combination of different models/techniques.

The description of the effect of the electronic excitation on the material properties is typically performed by means of computationally expensive electronic structure calculations, e.g., [23–36]. Simulations based on electronic structure calculations provide information on the changes in the interatomic bonding and the ultrafast atomic dynamics induced by the electronic excitation. The size of the systems used in electronic structure calculations, however, is typically limited to several hundreds of atoms and does not allow for a realistic representation of the transition from the electronic excitation to the *collective atomic dynamics* responsible for the structural transformations in the irradiated material.

Continuum-level simulations, on the other hand, are often used to study the laser heating, melting, evaporation, and ablation on realistic, experimental time and length scales. The most straightforward and computationally efficient continuum approach is based on the solution of a set of partial differential equations describing the laser energy deposition and evolution of temperature in the irradiated target. Various descriptions of melting, resolidification, surface vaporization, and ablation can be incorporated into such models, albeit at a rather simplified level. In particular, laser melting and resolidification are often described with a phase-change model based on an assumption of local equilibrium at the solid–liquid interface (heat-flow limited, interface kinetics formulated within the framework of the Stephan problem), e.g., [37–39], or using a kinetic equation relating the interface velocity to the interface temperature, e.g., [40–44]. The latter nonequilibrium kinetic description has been shown to be necessary for subnanosecond pulses, when

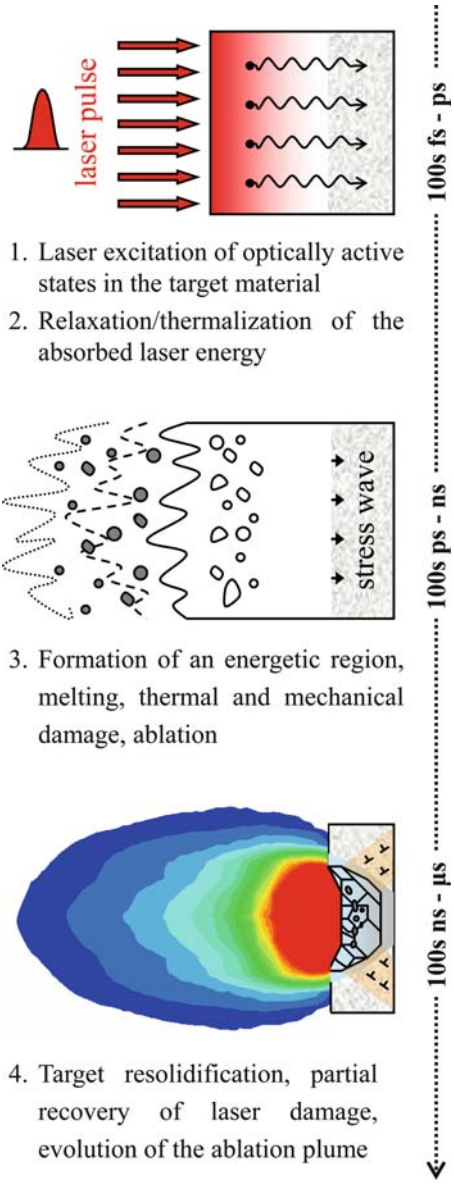

Fig. 3.1. Schematic representation of processes involved in short-pulse laser interactions with materials

a fast thermal energy flow to/from the liquid–solid interface creates conditions for significant overheating/undercooling of the interface [43, 44]. The material removal from the target can be incorporated into continuum models in the form of surface or volumetric vaporization models, e.g., [45–49],

whereas the expansion of the vaporized plume is commonly described by solving gas dynamics equations, e.g., [45–49] or using the Direct Simulation Monte Carlo (DSMC) technique, e.g., [50–55]. Hydrodynamic computational models based on multiphase equations-of-state have also been used for simulation of laser melting, spallation, and ablation [56–62]. The empirical equations-of-state provide a powerful framework for the description of the evolution of the thermodynamic parameters of the material (temperature, pressure, density, internal energy), as well as the conditions for the laser-induced phase transitions.

The common strength of the continuum models is in their computational efficiency and the ability to simulate laser-induced processes at experimental time and length scales. The highly nonequilibrium nature of the processes induced in the target material by the fast laser energy deposition, however, is challenging some of the basic assumptions of the continuum descriptions that are commonly designed based on the equilibrium material behavior and properties. Although incorporation of kinetic models and metastable states, e.g., [43, 44, 60, 61], is possible within the continuum approach, the predictive power of the models is limited by the necessity to make a priori assumptions on the mechanisms and kinetics of all the processes that may take place during the simulation. The investigation of the generation of crystal defects and microscopic mechanisms of laser melting, nucleation and growth of voids in photomechanical spallation, the characteristics of the explosive volume ablation and the parameters of the ejected multicomponent and multiphase ablation plume is difficult if not impossible with continuum models.

In a situation where the continuum modeling of laser–materials interactions is hindered by the complexity and the highly nonequilibrium nature of the phenomenon, the classical molecular dynamics (MD) computer simulation technique has emerged as a promising alternative approach, which is capable of providing atomic-level insights into the laser-induced processes. A quickly expanding range of applications of MD simulations includes investigations of laser-induced thermoelastic deformation, melting, and resolidification [63–74]; photomechanical damage and spallation [65, 68, 70, 75–82]; as well as laser ablation of various material systems [70, 78, 79, 83–115].

In the remaining part of this chapter, the capabilities and limitations of MD simulations of laser–materials interactions are discussed and illustrated by the results obtained in several recent computational studies. The basic ideas of the classical MD method and some of the recent developments of computational methodology that enable simulations of laser interactions with molecular systems and metals are presented next, in Sect. 3.2. Some of the results obtained in MD simulations of laser-induced generation of crystal defects, melting, photomechanical spallation, and ablation are discussed in Sect. 3.3. Finally, in Sect. 3.4, some of the promising directions for future computational exploration are discussed.

3.2 Molecular Dynamics Method for Simulation of Laser–Materials Interactions

In this section, we start from a brief introduction to the classical MD method and highlight the advantages and limitations of the MD technique with respect to addressing research questions relevant to laser ablation and laser material-processing applications. The MD models developed for simulation of laser interaction with molecular systems and metals are presented next, followed by a discussion of the boundary conditions that can provide a realistic description of the energy dissipation from the absorption region to the bulk of the target.

3.2.1 Molecular Dynamics Method

Molecular dynamics (MD) is a computer simulation technique that allows one to predict the time evolution of a system of interacting particles (atoms, molecules, granules). A detailed discussion of this method and the areas of its applicability can be found in several books devoted to atomistic simulation techniques, e.g., [116,117]. Briefly, MD allows one to follow the evolution of a system of N particles in time by solving a set of classical equations of motion for all particles in the system,

$$m_i \frac{\mathrm{d}^2 \mathbf{r}_i}{\mathrm{d}t^2} = \mathbf{F}_i, i = 1, 2, \ldots, \mathrm{N}, \tag{3.1}$$

where m_i and $\mathbf{r}_i$ are the mass and position of a particle i and $\mathbf{F}_i$ is the force acting on this particle due to the interaction with other particles in the system. The force acting on the i^{th} particle at a given time can be obtained from the interparticle interaction potential $U(\mathbf{r}_1, \mathbf{r}_2, \mathbf{r}_3, \ldots, \mathbf{r}_N)$ that, in general, is a function of the positions of all the particles:

$$\mathbf{F}_i = -\boldsymbol{\nabla}_i U\left(\mathbf{r}_1, \mathbf{r}_2, \mathbf{r}_3, \ldots, \mathbf{r}_N\right). \tag{3.2}$$

Once the initial conditions (initial positions and velocities of all particles in the system) and the interaction potential are defined, the equations of motion, (3.1), can be solved numerically. The result of the solution is the trajectories (positions and velocities) of all the particles as a function of time, $\mathbf{r}_i(t), \mathbf{v}_i(t)$, which is the only direct output of an MD simulation. From the trajectories of all particles in the system, one can easily calculate the spatial and time evolution of structural and thermodynamic parameters of the system. For example, the atomic-level analysis of the development of the defect structures or phase transformations can be performed and related to the changes in temperature and pressure in the system.

The main strength of the MD method is that the only input in the model is the function describing the interparticle interaction, $U(\mathbf{r}_1, \mathbf{r}_2, \mathbf{r}_3, \ldots, \mathbf{r}_N)$,

and no assumptions are made about the character of the processes under study. This is an important advantage that makes the MD method to be capable of discovering new physical phenomena or processes in the course of a "computer experiment." Moreover, unlike real experiments, the analysis of fast nonequilibrium processes in MD simulations can be performed with unlimited atomic-level resolution, providing complete information on the phenomena of interest. The predictive power of the MD method, however, comes at a price of a high computational cost, which imposes severe limitations on the time and length scales accessible for the simulation. The record length-scale MD simulations of systems containing more than 10^{11} atoms (micron-size cubic samples) have been performed with the use of thousands of processors on one of the world's largest supercomputers [118], whereas long time-scale (up to hundreds of microseconds) simulations of protein folding have been performed through distributed computing [119].

The limitations on the time- and length scales that are accessible for MD simulations present a serious challenge for the modeling of laser-induced processes that typically involve a collective motion of a large number of atoms or molecules in the surface region of the irradiated target. Moreover, since the electrons and quantum effects are not explicitly included in the classical MD, the optical properties of the irradiated material cannot be obtained in the course of the simulation, but have to be assumed in advance and provided as input to the model. Thus, the design of novel approaches aimed at extending the time- and/or length-scales of MD simulations and incorporating a description of the laser excitation into the MD model is required for an adequate modeling of laser–materials interactions. Two examples of computational models developed for MD simulations of laser interactions with molecular systems and metals are discussed next, in Sects. 3.2.2 and 3.2.3.

3.2.2 Coarse-Grained MD Model for Simulation of Laser Interactions with Molecular Systems

In an atomic-level MD model, a typical small molecule or a monomer unit can include tens of atoms, and a time-step of the integration of the equations of motion of 0.1 fs or smaller must be used to follow high-frequency atomic vibrations. In order to overcome the limitations of the atomistic MD model and to address collective processes responsible for laser-induced material modification or ablation, a coarse-grained "breathing sphere" MD model has been developed [98, 101].

The breathing sphere model assumes that each molecule can be represented by a single particle, Fig. 3.2a. The parameters of interparticle interaction are chosen to approximately reproduce the physical properties of a molecular target. The equilibrium distance in the interparticle potential is defined as the distance between the edges of the spherical particles rather than their centers, Fig. 3.2c. This choice of equilibrium distance is based on the physical

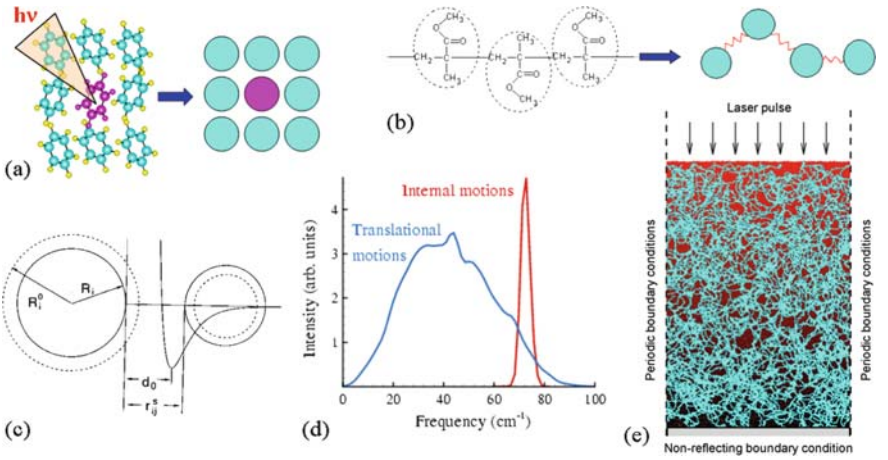

Fig. 3.2. Schematic representation of the approximations used in the design of coarse-grained breathing sphere (**a**) and bead-and-spring (**b**) MD models. Potential of intermolecular interaction in the breathing sphere model is shown in (**c**), where R_i^0 and R_i are the equilibrium and instantaneous radii of the particle i; d_0 and r_{ij}^s are the equilibrium and instantaneous distances between the edges of the spherical particles. The radii of the breathing spheres, R_i, are dynamic variables for which equations of motion are solved during the simulation. Vibrational spectrum of an organic solid represented by the breathing sphere model and the vibrational peak corresponding to the internal breathing mode are shown in (**d**). Schematic sketch of a simulation setup for modeling of laser ablation of a 3 wt.% polymer solution is shown in (**e**). The polymer chains are shown in light grey color and are superimposed on top of the image of matrix molecules shown in the background. Figures shown in (**c**) and (**d**) are from [98] and the image in (**e**) is from [113]

concept that the sublimation or cohesive energy of an organic solid is governed primarily by the interactions among atoms on the outside of the molecule. This representation of intermolecular interactions allows an easy means of simulating multicomponent molecular systems [98, 102, 105, 106].

In order to simulate molecular excitation by photon absorption and vibrational relaxation of the excited molecules, an additional internal degree of freedom is attributed to each molecule. The internal degree of freedom, or breathing mode, is implemented by allowing the particles to change their sizes. In the case of UV laser irradiation, the breathing mode can be considered as the recipient of the energy released by an internal conversion from electronically excited states. The parameters of a potential function attributed to the internal motion control the characteristic frequency of the breathing mode, Fig. 3.2d; and, as a result, define the rate of the conversion of the internal energy of the molecules excited by the laser to the translational and internal motions of the surrounding molecules. The rate of the vibrational relaxation of excited molecules is an input parameter in the model and can be either

estimated from pump-probe experiments [120, 121] or obtained in atomistic [122] or *ab initio* [123] MD simulations.

The laser irradiation is simulated by vibrational excitation of molecules that are randomly chosen during the laser pulse duration within the penetration depth appropriate for a given wavelength. Vibrational excitation is modeled by depositing a quantum of energy equal to the photon energy into the kinetic energy of internal motion of a given molecule. An alternative result of the photon absorption, photofragmentation of the excited molecule into fragments that can subsequently participate in chemical reactions, can also be reproduced within the model [78, 106, 111]. A description of the processes leading to the ionization of molecules in laser ablation has recently been incorporated into the breathing sphere model and the mechanisms responsible for the ion formation in matrix-assisted laser desorption ionization (MALDI) mass spectrometry technique have been explored [112].

In order to enable simulations of laser interaction with polymer solutions [107, 113, 114, 124–126], the breathing sphere model has recently been combined with the bead-and-spring model, commonly used in polymer modeling [127]. In the bead-and-spring model, schematically illustrated in Fig. 3.2b, the "beads" representing the functional groups of a polymer molecule (monomers) are connected by anharmonic springs with strengths appropriate for chemical bonding. An example of the computational setup used in simulations of laser ablation of polymer solutions [113, 124, 125] is given in Fig. 3.2e.

Since both the breathing sphere model and the bead-and-spring model adopt a coarse-grained representation of molecules, in which each molecule or monomer unit is represented by a single particle, the system size can be sufficiently large to reproduce the collective dynamics in a molecular system leading to laser ablation or damage. Moreover, since explicit atomic vibrations are not followed, the time-step in the numerical integration of the equations of motion can be much longer and the dynamics in the irradiated sample can be followed for as long as nanoseconds. The limitations of the breathing sphere model are related to the approximation of all the internal degrees of freedom of a molecule by one internal mode. The rates of intermolecular energy transfer cannot be studied within the model, but have to be specified through the input parameters, as discussed earlier. The accuracy in quantitative description of the thermodynamic and transport properties of the materials represented at the coarse-grained level is limited, and the model is appropriate for investigation of general, rather than material-specific, characteristics of the laser-induced processes. A smaller number of degrees of freedom in the model system should also be taken into account when performing a quantitative comparison with experimental data, e.g., of the threshold fluence for the ablation onset [79, 103].

3.2.3 Combined Continuum-Atomistic Model for Simulation of Laser Interactions with Metals

In metals, laser light is absorbed by the conduction band electrons. The deposited energy quickly, within femtoseconds, is equilibrated among the electrons and, more slowly, is transferred to the lattice vibrations. The later process is controlled by the strength of the electron–phonon coupling and can take from fractions of a picosecond to several tens of picoseconds. Finally, a thermal equilibrium is established between the electrons and phonons, and the conventional heat conduction equation can be used to describe the heat flow into the bulk of the irradiated target. The classical MD technique does not include an explicit representation of electrons and, therefore, cannot be used, in its conventional formulation, for simulation of the laser light interaction with the target material, the relaxation/thermalization of the absorbed laser energy, and the fast electron heat conduction to the bulk of the irradiated target.

To enable atomic-level simulations of processes involving electronic excitations of metal targets by short-pulse laser irradiation (or energetic ion bombardment), several computational approaches have been proposed [64, 65, 89, 108, 128, 129]. In particular, the model described in [65] combines classical MD method with a continuum description of the laser excitation and subsequent relaxation of the conduction band electrons, based on the so-called two-temperature model (TTM) [130]. In the original TTM, the time evolution of the lattice and electron temperatures, T_l and T_e, is described by two coupled nonlinear differential equations. In the combined TTM–MD method, schematically illustrated in Fig. 3.3, MD partially substitutes the TTM equation for the lattice temperature. The diffusion equation for the electron temperature is solved by a finite difference method simultaneously with MD integration of the equations of motion of atoms. The electron temperature enters a coupling term that is added to the MD equations of motion to account for the energy exchange between the electrons and the lattice. The MD method is used only in the very surface region of the target, where active processes of laser melting, resolidification, and/or ablation take place, whereas the diffusion equation for the electron temperature is solved in a much wider region affected by the thermal conduction. A special pressure-transmitting boundary condition applied at the bottom of the MD part of the computational region, as well as the periodic boundary conditions imposed in the directions parallel to the surface, is briefly discussed later, in Sect. 3.2.4. In the part of the computational cell beyond the MD region (left part in Fig. 3.3), the energy exchange between the electrons and the lattice is described by the conventional TTM.

The hybrid continuum-atomistic model, briefly described above, combines the advantages of TTM and MD methods. TTM provides an adequate description of the laser energy deposition into the electronic system, the energy exchange between the electrons and phonons, and the fast electron heat

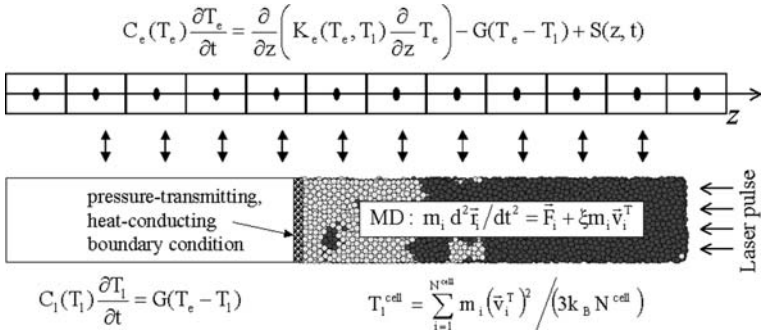

Fig. 3.3. Schematic representation of the combined continuum-atomistic model for simulation of laser interaction with a metal target. The evolution of electron temperature, T_e, is described by a nonlinear differential equation, whereas the atomic motions are described by the MD method with an additional term, $\xi m_i \mathbf{v}_i^T$, added to the ordinary MD equations of motion to account for the electron–phonon coupling. Spatial discretization in the continuum model (typically $\sim$1 nm) and size of the atomistic region are not drawn to scale. The cells in the finite difference discretization are related to the corresponding volumes of the MD system and the local lattice temperature, T_l^{cell}, is defined for each cell from the average kinetic energy of thermal motion of atoms. Thermal velocity of an atom is defined as $\mathbf{v}_i^T = \mathbf{v}_i - \mathbf{v}^c$, where $\mathbf{v}_i$ is the actual velocity of an atom i and $\mathbf{v}^c$ is the velocity of the center of mass of a cell to which the atom i belongs. A Gaussian temporal profile, $S(z,t)$, is used to describe the laser excitation of the conduction band electrons. The expansion, density variations and, at higher fluences, disintegration of the irradiated target predicted in the MD part of the model are accounted for in the continuum part of the model. A complete description of the combined TTM–MD model is given in [65]

conduction in metals, whereas the MD method is appropriate for simulation of rapid nonequilibrium phase transformations, damage, and ablation.

The results of the recent investigation of the electron temperature dependence of the electron–phonon coupling factor G, the electron heat capacity C_e, and the heat conductivity K_e (thermophysical material properties included in the TTM equation for the electron temperature, see Fig. 3.3) suggest that the effect of the thermal excitation from the electron states below the Fermi level should be accounted for in a model aimed at a quantitative description of the laser-induced processes in metals [131–134]. Indeed, a computational analysis based on the first-principles electronic structure calculations of the electron density of states reveals that these thermophysical materials properties are very sensitive to details of the electronic structure of the material and can exhibit large deviations (up to an order of magnitude) from the commonly used approximations of a linear temperature dependence of the electron heat capacity and a constant electron–phonon coupling. A number of practically important characteristics of the laser–material interactions, such as the threshold fluences for the onset of melting and ablation, the strength of the laser-induced stress wave, the emission of electrons from the irradiated

surface, and the depth of the melting and/or heat-affected zone, can all be significantly altered by the transient changes of the thermophysical properties occurring during the time of electron–phonon equilibration. It has been shown, in particular, that incorporation of the new electron temperature dependences of the thermophysical properties [133, 134] into TTM or TTM–MD models results in an improved agreement between the computational predictions and experimental observations [20, 131, 132, 135].

In the examples considered in Sect. 3.3 of this chapter, the interatomic interactions in the MD part of the TTM–MD model are described by the embedded atom method (EAM) potential [136, 137] that provides a computationally simple but rather realistic description of bonding in metallic systems. In particular, the functional form and parameters of the EAM potential for Ni, Al, Cu, and Au are given in [138], whereas a recently developed potential for Cr is described in [74].

3.2.4 Boundary Conditions: Pressure Waves and Heat Conduction

The severe limitations on the length scales in MD method make it impossible to directly simulate processes occurring within the whole laser spot. For a laser spot of 10–100 μm in diameter and an ablation depth of 10–100 nm, one can estimate that the number of molecules/atoms ejected from an irradiated target in a single laser shot is in the range from tens of billions to trillions. These numbers are much beyond the limits of the MD simulation technique (see Sect. 3.2.1). In this situation, the MD computational cell is typically assumed to represent a local volume within the laser spot and the material response to local laser energy deposition is investigated, as schematically shown in Fig. 3.4. The periodic boundary conditions in the lateral directions, parallel to the surface of the target, are used in this case to reproduce the interaction of molecules or atoms in the MD computational cell with the surrounding material. This approach is appropriate for a situation in which the laser spot diameter is much larger than the depth of the laser energy deposition, so that any effects related to the lateral variations of the irradiation and thermal conditions can be neglected and the simulated part of the system remains laterally confined by the surrounding material during the time of the simulation. The information on the material ejection from the whole laser spot can then be obtained by integrating over the results of a series of MD simulations performed for a range of "local fluences," Fig. 3.4.

In the direction normal to the surface of the irradiated target, a free boundary condition, allowing for a natural expansion of the irradiated target and the ejection of atoms, molecules, and clusters in laser ablation, is the natural choice for the irradiated (top) surface. More complex boundary conditions, however, accounting for the thermal conduction and pressure wave propagation from the absorption region deeper into the bulk of the target, have to be used at the bottom of the MD computational cell.

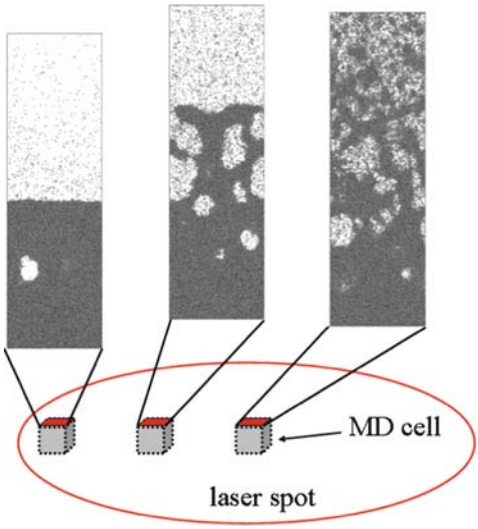

Fig. 3.4. Schematic illustration of the local areas represented in MD simulations of laser ablation at different locations within a laser spot. Snapshots used in this figure are from simulations of laser interactions with a molecular target [78]

In order to evaluate the necessity for the introduction of the heat-conductive and pressure-transmitting boundary conditions, one can consider characteristic times of the heat transfer and pressure wave propagation across a typical size of the MD computational cell, $L_{\mathrm{MD}} \approx 100\,\mathrm{nm}$. The timescale of the heat conduction across the computational cell can be evaluated as $\tau_{\mathrm{th}} \approx \left(L_{\mathrm{MD}}^2\right) / \left(2D_{\mathrm{T}}\right)$, where D_{T} is the thermal diffusivity of the target material. For molecular systems $D_{\mathrm{T}} \approx 10^{-7}\,\mathrm{m^2\,s^{-1}}$, and the timescale of the heat conduction is $\tau_{\mathrm{th}} \approx 50\,\mathrm{ns}$, much longer than the time-scale of a typical MD simulation. In metals, however, the heat conduction, dominated by the electron heat transport, is much larger, e.g., $D_{\mathrm{T}} \approx 10^{-4}\,\mathrm{m^2\,s^{-1}}$ for gold. This yields $\tau_{\mathrm{th}} \approx 50\,\mathrm{ps}$, a time that is shorter than the time needed for an adequate simulation of laser-induced structural transformations. Therefore, we can conclude that, while the effect of heat transfer through the bottom of a sufficiently large computational cell can be neglected in simulations of molecular systems, the boundary conditions in simulations of laser interactions with metals must account for the heat conduction. The combined TTM–MD model, discussed in Sect. 3.2.3, provides a natural description of the electron heat conduction from the surface region of the target, represented with atomic-level resolution, to the deeper part of the target, represented at the continuum level, Fig. 3.3. Indeed, a seamless transition in the temperature field from the atomistic to the continuum regions can be seen in Fig. 3.9 (Sect. 3.3.3), illustrating the evolution of temperature in a simulation performed for a bulk Ni target irradiated with a 1 ps laser pulse.

The pressure waves, generated as a result of the relaxation of laser-induced thermoelastic stresses and, above the threshold for the ablation onset, recoil pressure from the ejected material, present an additional challenge for simulations of short-pulse laser–materials interactions. In order to simulate a propagation of the laser-induced pressure wave into the bulk of the sample, the size of the MD computational cell should be increased linearly with the time of the simulation. For times longer than a hundred of picoseconds, the size of the model required to follow the wave propagation becomes computationally prohibitive. If large computational cells are not used, however, artificial border effects can interfere with the simulation results, as both rigid and free boundary conditions lead to the complete reflection of the pressure wave [78, 82]. The free boundary condition at the bottom of the computational cell is appropriate for simulations of laser interaction with free-standing films [65–68, 70–72, 75, 76, 82, 91], whereas the rigid boundary condition can be related to experiments performed for a thin absorbing layer deposited on a hard substrate [139]. In most cases, however, we are interested in much larger systems for which the effect of the pressure wave reflection has to be avoided. To enable the simulations of laser interactions with bulk systems, special pressure-transmitting boundary condition based on an analytical evaluation of the forces acting on atoms/molecules in the boundary region from the outer "infinite medium" has been developed [140, 141]. The energy that is carried away by the stress wave though the pressure-transmitting boundary condition can be monitored, allowing for a control over the energy conservation in the model [69]. The nonreflecting boundary conditions have been successfully used in simulations of laser melting, ablation, and damage for different target materials in which both planar, e.g., [69, 78–82, 89, 92, 93, 103–113] and spherical [142] pressure waves are generated. An illustration of the nonreflective propagation of the pressure wave from the atomistic to the continuum parts of the combined TTM–MD model can be seen in Fig. 3.9 (Sect. 3.3.3).

3.3 Simulations of Laser-Induced Structural and Phase Transformations

The MD method allows one to perform a detailed analysis of the laser-induced processes in which thermodynamic parameters of the system can be correlated with microscopic dynamics at the atomic level. In this section, the ability of the MD method to provide insights into the mechanisms of laser–materials interactions is demonstrated by a representative set of recent computational results obtained in simulations of laser-induced generation of crystal defects, melting, photomechanical spallation, and ablation.

3.3.1 Generation of Crystal Defects

The understanding of the mechanisms and driving forces responsible for laser-induced generation of crystal defects is important for the advancement of laser processing applications aimed at controlled modification of surface microstructure. MD simulations are capable of providing detailed atomic-level information on the elementary processes responsible for the generation and evolution of defect configurations in irradiated targets. To illustrate this capability and highlight the sensitivity of the laser-induced defect structures to the type of the crystal structure of the target, the results of simulations performed for two metals with different crystal structures, body-centered cubic (bcc) Cr and face-centered cubic (fcc) Ni, are discussed in this section.

The fast structural changes in a Cr target irradiated with a 200-fs laser pulse have been analyzed in [74] based on the results of TTM–MD simulations. The snapshots of atomic configurations taken at different times of a simulation performed at an absorbed fluence of $638\,\mathrm{J\,m^{-2}}$ (just above the threshold for surface melting) are shown in Fig. 3.5a. Only atoms that belong to the liquid phase or are located in the vicinity of crystal defects, are shown in the snapshots, with all the atoms that have local atomic surroundings (and corresponding values of the potential energy) similar to the ones in the original bcc structure blanked. During the first 100 ps after the laser pulse, the irradiated target experiences transient melting and epitaxial resolidification of a thin (up to 3 nm) surface layer, which shows up in Fig. 3.5a as a layer of red atoms at 50 ps and reduces to a plane composed of atoms located at the surface of the recrystallized target by the time of 100 ps.

Another transient effect apparent from the snapshots shown in Fig. 3.5a is the appearance, expansion (up to 30 ps), retraction, and disappearance (by 115 ps) of a complex pattern of atomic planes with elevated energy. Detailed analysis of the atomic configurations reveals that these planes correspond to the intrinsic stacking faults generated as a result of multiple internal shifts along {110} crystallographic planes by displacement vectors $a/8 < 110 >$ (where a is the lattice parameter). The generation of the stacking faults is activated by the rapid uniaxial expansion of the crystal in the direction normal to the irradiated surface. Calculations of the generalized stacking fault energy suggest, in agreement with earlier studies [143], that the intrinsic stacking faults are unstable in an unstrained bcc crystal but can be stabilized by a uniaxial expansion of the crystal. Indeed, the appearance of the stacking faults correlates with the lattice expansion associated with the initial relaxation of the laser-induced stresses. All stacking faults disappear by ∼115 ps, shortly after the laser-induced tensile stress wave leaves the surface region of the target [74].

The disappearance of the stacking faults makes the presence of a large number of vacancies clearly visible in the surface region of the target, e.g., snapshot shown for 450 ps in Fig. 3.5a. With the visualization method used in Fig. 3.5a, where only atoms with elevated potential energy are shown, each

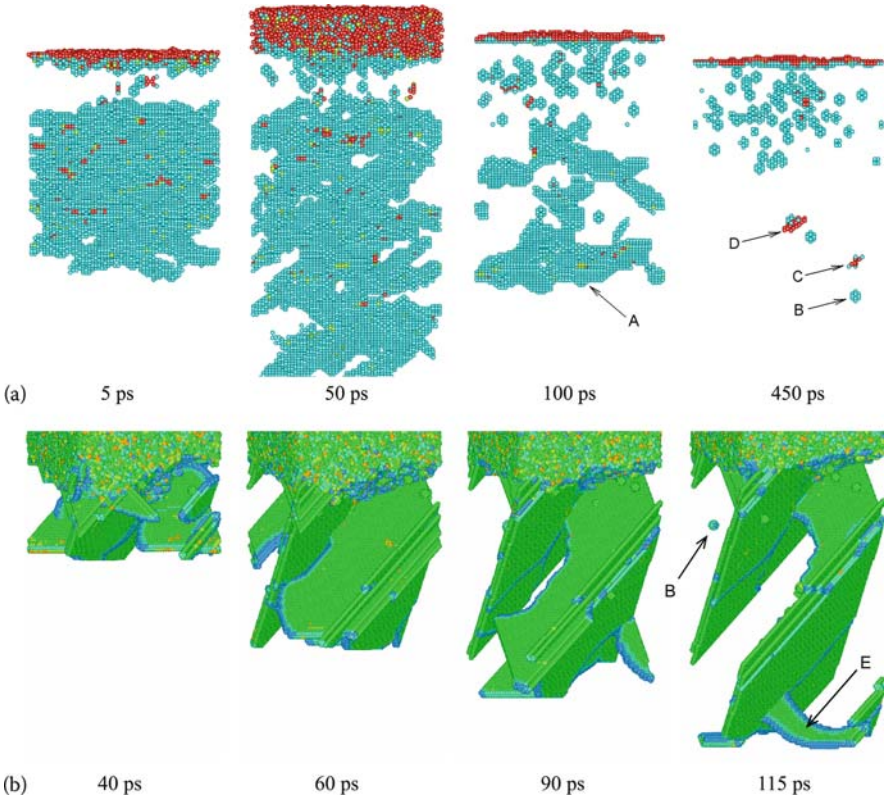

Fig. 3.5. Snapshots of the surface regions of atomic configurations obtained in TTM–MD simulations of bcc Cr (**a**) and fcc Ni (**b**) targets irradiated with a short pulse laser. The absorbed laser fluences and pulse durations are 638 J m^{-2} and 200 fs for Cr, and 645 J m^{-2} and 1 ps for Ni targets. The snapshots are shown down to the depth of 20 nm below the level of the initial surface in (**a**) and for a region located between 30 and 60 nm below the level of the initial surface in (**b**). The atoms are colored according to their potential energies in (**a**) and the centrosymmetry parameter in (**b**), with atoms that belong to local configurations corresponding to the original bcc (**a**) or fcc (**b**) structure blanked to expose crystal defects. Typical defect configurations marked in the snapshots are "A" – stacking fault with a displacement vector of $a/8<110>$, "B" – a vacancy, "C" – an interstitial in a <110>-dumbbell configuration, "D" – a four <111>-crowdion interstitial cluster, and "E" – a dislocation with a Burgers vector of $a/2<110>$, dissociated into two $a/6<112>$ Shockley partial dislocations connected by a stacking fault ribbon. The snapshots shown in (**a**) are from [74]

vacancy appears as a cluster of 14 atoms that includes the eight nearest neighbors and six second-nearest neighbors of the missing atom. The number of vacancies observed in the top 5 nm surface region of the target at 450 ps corresponds to a very high vacancy concentration, more than 10^{-3} vacancies per

lattice site. The thermally activated generation of vacancy-interstitial pairs during the laser-induced temperature spike serves as the initial source of the point defects. Due to the high mobility of self-interstitials, they quickly escape to the melting front or the free surface of the target, leaving behind a large number of vacancies (only one individual interstitial and one cluster of four interstitials arranged in a mobile <111>-crowdion configuration can be identified in a snapshot shown for 450 ps in Fig. 3.5a). A significant number of vacancies are also produced at the advancing solid–liquid interface during the fast resolidification process.

The strong temperature gradient created in the surface region of the target by the short-pulse laser irradiation, and the associated ultrafast cooling rates exceeding $5 \times 10^{12}\,\mathrm{K\,s^{-1}}$ at the time of resolidification, provide the conditions for stabilization of the highly nonequilibrium vacancy concentration. Indeed, an analysis of the long-term evolution of the vacancy configuration, performed in [74], suggests that the average vacancy diffusion length during tens of nanoseconds after the end of the TTM–MD simulation is very small, on the order of an interatomic distance. The configuration of mostly individual vacancies observed at the end of the TTM–MD simulation is, therefore, unlikely to undergo any significant changes during the remaining part of the cooling process.

The processes responsible for the generation of crystal defects in fcc Ni target exhibit both similarities and differences with the ones discussed above for bcc Cr target. The formation of vacancy-interstitial pairs followed by the fast escape of the interstitials is observed in both Ni and Cr targets and proceeds in a qualitatively similar manner. An important difference between the simulations performed for the two materials is a massive generation of partial dislocations observed for Ni targets, e.g., Fig. 3.5b. This observation can be related to the existence of stable low-energy stacking faults and 12 close-packed $\{111\}\ <1\bar{1}0>$ slip systems with small resistance to the motion of dislocations (low Peierls stress) in fcc crystals. Unlike the transient appearance of the unstable stacking faults in Cr, the stacking faults left behind by the partial dislocations propagating from the melting front in the Ni target are stable and have relatively low energy ($110\,\mathrm{mJ\,m^{-2}}$ is predicted by the EAM Ni potential, in a reasonable agreement with the experimental value of $125\,\mathrm{mJ\,m^{-2}}$ [144]). Interactions between the dislocations propagating along the different slip planes result in the formation of immobile dislocation segments (the so-called stair-rod dislocations) that, together with the fast cooling of the surface region of the target, stabilize the dislocation configuration generated during the initial spike of temperature and thermoelastic stresses.

The supersaturation of the surface region of an irradiated target with vacancies, observed for both Ni and Cr targets, may result in the formation of nanovoids and degradation of the mechanical properties of the surface region of the target in the multipulse irradiation regime. The generation of crystal defects may be, thus, related to the incubation effect, when the laser fluence threshold for ablation/damage decreases significantly with increasing number

of laser pulses applied to the same area, e.g., [145–149]. The high density of vacancies generated in the surface region should also play an important role in the redistribution of impurities or mixing/alloying in multicomponent or composite targets. The generation of dislocations and, in particular, dislocation reactions leading to the formation of immobile dislocation configurations should result in hardening of the surface region of the target.

3.3.2 Mechanisms and Kinetics of Laser Melting

Most of the methods of laser surface modification involve melting and subsequent resolidification of a surface region. It has been well established that melting starts at surfaces and internal crystal defects under minor superheating conditions or even below the equilibrium melting temperature [150, 151]. After heterogeneous nucleation of the liquid phase, the liquid–solid interface propagates into the bulk of the solid, precluding any significant superheating and making observation of an alternative mode of melting, homogeneous nucleation in the bulk of a superheated crystal, difficult. The extremely high heating rates achievable with short-pulse laser irradiation, however, create the conditions for competition between the heterogeneous and homogeneous melting mechanisms and provide unique opportunities for the investigation of the kinetic limits of achievable superheating. Moreover, the emerging time-resolved electron and X-ray diffraction experimental techniques are capable of probing the transient atomic dynamics in laser melting with subpicosecond resolution [14–22]. The complexity of the fast nonequilibrium phase transformation, however, hinders the direct translation of the diffraction profiles to the transient atomic structures.

MD simulations are well suited for investigation of the ultrafast laser melting phenomenon and are capable of providing detailed atomic-level information needed for a reliable interpretation of experimental observations. In particular, the kinetics and mechanisms of laser melting have been investigated in a series of TTM–MD simulations performed for Ni, Au, and Al thin films and bulk targets irradiated by short, from 200 fs to 150 ps, laser pulses [65–72,109,132]. The relative contributions of the homogeneous and heterogeneous melting mechanisms have been analyzed and related to the irradiation conditions. Except for the fluences close to the threshold for surface melting, the heterogeneous melting (melting front propagation from the surface) is found to make very limited contribution to the overall melting process, with homogeneous nucleation of multiple liquid regions being the dominant melting mechanism [65,66,71]. This observation has been supported by the results of recent large-scale TTM–MD simulations aimed at establishing the maximum velocity of the melting front propagation in metals [152]. A surprising result from this study is that the maximum velocity of the melting front just below the limit of the crystal stability against homogeneous melting is below 3% of the speed of sound, more than an order of magnitude lower than commonly assumed in interpretation of the results of laser melting experiments,

e.g., [10, 14, 153]. The relatively low maximum velocity of the melting front, revealed in the simulations, has direct implications for interpretation of the experimental data on the kinetics of melting. For example, for thin 20-nm Au films used in recent time-resolved electron diffraction experiments [20,154], the melting time shorter than 70 ps would clearly point to the major contribution of the homogeneous nucleation to the melting process [71, 132].

A schematic map of the melting mechanisms shown in Fig. 3.6 can provide guidance in the analysis of the relative contributions of different processes to laser melting. The heterogeneous melting starts from the free surface(s) of the target as soon as the temperature exceeds the equilibrium melting temperature, T_m. The equilibrium melting temperature is changing with pressure according to the Clapeyron equation (increases with increasing pressure for metals having positive volume change on melting). As discussed earlier, the melting front propagation is relatively slow and the surface region of the irradiated target can be easily overheated significantly above the equilibrium melting temperature, up to the limit of superheating shown by the dashed line in Fig. 3.6. The temperature of the maximum superheating, T_s, is defined as a temperature at which melting starts within tens of picoseconds in a simulation performed for a perfect crystal with three-dimensional periodic boundary conditions (no external surfaces) under conditions of constant hydrostatic pressure. The values of the maximum superheating, $(T_s–T_m)/T_m$, predicted in MD simulations for different close-packed metals vary from 0.19 to 0.30 [155] and are somewhat smaller, below 0.15, for bcc metals [74, 156]. In the case of EAM Ni used in Fig. 3.6, the maximum superheating gradually increases from 0.21 to 0.25 as pressure increases from –5 GPa to 10 GPa.

In the area of the pressure–temperature field above the limit of superheating (red area in Fig. 3.6), rapid nucleation and growth of liquid regions inside the superheated crystal are responsible for the melting process. Note that the homogeneous melting observed above the maximum superheating does not follow the classical picture of a homogeneous phase transition – the nucleation and growth of well-defined spherical liquid regions. Rather, the melting in this regime proceeds as a collapse of the lattice superheated above the limit of its stability and takes place within just several picoseconds (several periods of atomic vibrations). Actually, the "classical" homogeneous melting has never been observed in laser melting simulations performed so far and the image showing two compact liquid regions in Fig. 3.6 is taken from a simulation of a slow heating of a crystal under well-controlled temperature and pressure conditions. Indeed, one can expect that the fast evolution of the temperature and pressure induced by short-pulse laser irradiation would readily overshoot the narrow region close to the limit of superheating (shown by green color in Fig. 3.6) where the "classical" homogeneous melting may be expected. Moreover, the temperature of the onset of homogeneous melting (the limit of superheating) can be significantly reduced by anisotropic lattice distortions associated with the relaxation of the laser-induced thermoelastic stresses [66]. Above the limit of superheating, the melting happens so fast that there is no

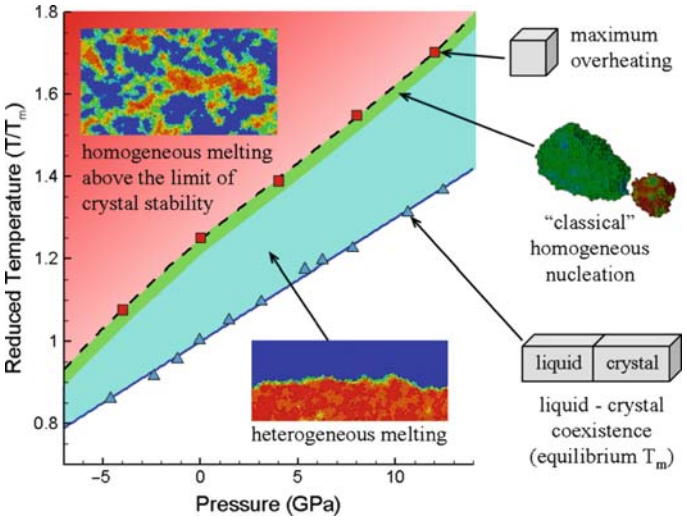

Fig. 3.6. Pressure/temperature conditions for equilibrium and nonequilibrium melting observed in simulations of laser interactions with metal targets. Blue triangles correspond to the conditions of equilibrium melting obtained in liquid-crystal coexistence simulations. Red squares connected by the black dashed line correspond to the maximum overheating of a crystal observed in simulations performed with three-dimensional periodic boundary conditions and constant hydrostatic pressure. The areas of the pressure–temperature field corresponding to the ultrafast homogeneous melting above the limit of superheating, classical homogeneous melting by nucleation and growth of individual liquid regions, and heterogeneous melting by the melting front propagation from the surface are shown by red, green, and blue colors, respectively. The data points are calculated for the EAM Ni material

time for the system to minimize the interfacial energy for the rapidly evolving liquid regions.

A typical picture of the homogeneous melting above the limit of superheating is shown in Fig. 3.7, where the snapshots from a simulation of laser melting of a 20 nm Au film are shown along with the corresponding structure functions. The fluence used in this simulation is ∼75% above the fluence needed for the complete melting of a 20 nm Au film [71]. The small thickness of the film and the fast electron energy transport in Au [65,71,132] result in the even distribution of the electron temperature established shortly after the laser excitation. The electron–phonon energy transfer then leads to the increase of the lattice temperature. The lattice temperature exceeds the equilibrium melting temperature by more than 40% by the time of 6 ps, triggering a spontaneous homogeneous nucleation of a large number of small liquid regions throughout the film and a rapid collapse of the crystalline structure within the subsequent 3–4 ps ($T_s \approx 1.25T_m$ for the EAM Au). The visual analysis of the snapshots taken during the melting process shows that by ∼6 ps the growth of liquid regions starts at two free surfaces of the film, where the kinetic energy barrier

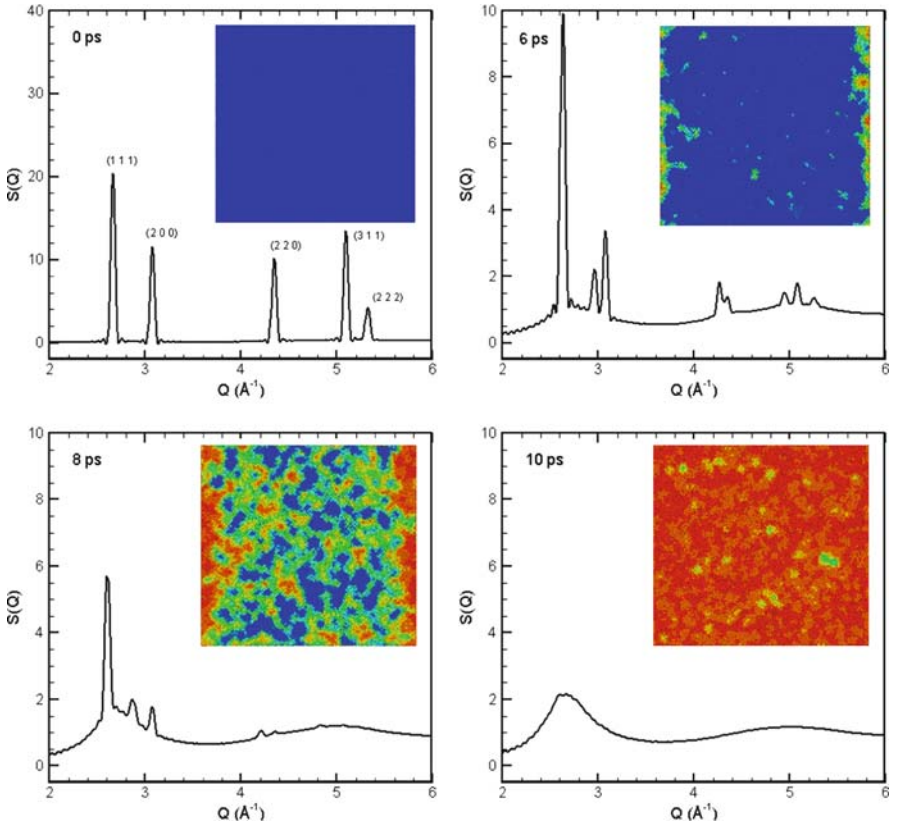

Fig. 3.7. Structure functions calculated for atomic configurations generated in a TTM–MD simulation of laser melting of a 20-nm Au film, irradiated with a 200-fs laser pulse at an absorbed fluence of 92.5 J m^{-2}. The corresponding snapshots of atomic configurations are shown as insets in the plots, with the laser pulse directed from the right to the left sides of the snapshots. Atoms in the snapshots are colored according to the local order parameter [65] – blue atoms have local crystalline surroundings and red atoms belong to the liquid phase. Zero time corresponds to a perfect fcc crystal at 300 K just before the laser irradiation. The effect of the thermal excitation of *d*-band electrons on the parameters of the TTM equation for the electron temperature [133] is included in this simulation. The snapshots are from Ref. [132]

is absent for the nucleation of the liquid phase. However, due to the fast rate of the lattice heating, the propagation of the melting fronts from the free surfaces of the film does not make any significant contribution to the overall melting process.

The calculation of the diffraction profiles and density correlation functions [71,72] provides a direct connection between the results of MD simulations and time-resolved diffraction experiments. The increasing amplitude of thermal

atomic vibrations (Debye–Waller factor), as well as shifts and splittings of the diffraction peaks due to the thermoelastic deformation of the film prior to melting, is found to be responsible for the initial decrease of the intensity of the diffraction peaks (from 0 to 6 ps in Fig. 3.7). The onset of the melting process at ∼6 ps leads to the complete disappearance of the crystalline diffraction peaks by the time of 10 ps, Fig. 3.7.

The simulation illustrated in Fig. 3.7 is performed for the irradiation conditions similar to the ones used in recent time-resolved electron diffraction measurements performed for 20 nm Au films [20, 154]. The disappearance of the diffraction peaks corresponding to the crystal structure is found to take place between 7 ps and 10 ps after the laser pulse. This experimental observation is in an excellent agreement with the simulation results illustrated in Fig. 3.7. Note that this agreement has only been achieved by accounting for the effect of the thermal excitation of *d* band electrons on the electron temperature dependence of the electron heat capacity and electron–phonon coupling [131–134] in the TTM–MD model. Earlier simulations, performed with the commonly used approximations of the constant electron–phonon coupling factor and the linear temperature dependence of the electron heat capacity, predict a much longer, ∼16 ps, delay time for the onset of melting [71, 132]. This observation supports the importance of accounting for the effects related to the thermal excitation of lower band electrons [133] for realistic modeling of laser-induced processes.

3.3.3 Photomechanical Spallation

The fast energy deposition in short-pulse laser processing application not only results in a sharp temperature rise in the surface region of the target but, unavoidably, generates strong thermoelastic stresses that can play an important role in defining the characteristics of laser melting, generation of crystal defects, and material ejection. The maximum values of the laser-induced stresses and the contribution of the so-called photomechanical effects to the material modification and damage are related to the condition of stress confinement [5, 78, 82, 157–160]. In systems with relatively slow heat conduction and fast thermalization of the deposited laser energy, the condition for the stress confinement is mainly defined by the laser penetration depth, L_p, and the laser pulse duration, τ_p. It can be written as $\tau_p \leq \tau_s \sim L_p/C_s$, where C_s is the speed of sound in the target material. In metals, the strength of the electron–phonon coupling and much faster electron heat conduction are additional factors that affect the maximum thermoelastic stresses that can be created in the target. The characteristic time of the energy transfer from the excited hot electrons to the lattice, τ_{e-ph}, and the diffusive/ballistic penetration depth of the excited electrons before the electron–phonon equilibration, L_c, define the condition for the stress confinement, $max\{\tau_p, \tau_{e-ph}\} \leq \tau_s \sim L_c/C_s$ [82].

The interaction of the laser-induced compressive stresses with the free surface of the irradiated sample can result in the generation of tensile stresses sufficiently high to cause mechanical fracture of a brittle material or promote cavitation and fragmentation in a metastable liquid. By analogy with the term "spallation," commonly used to describe the dynamic fracture that results from the reflection of a shock wave from a back surface of a sample [161–163], the material ejection (or partial separation of a surface layer) due to the laser-induced stresses is often called front-surface laser spallation. Although "cavitation" may be a more appropriate term when the photomechanical processes take place in the melted part of the target, in this chapter we use the term "front-surface laser spallation" for both solid and liquid/melted targets, as soon as the transient thermoelastic stresses play the dominant role in causing ablation/damage of the target. The processes of photomechanical front- and back-surface spallation are schematically illustrated in Fig. 3.8. Short-pulse laser irradiation occurring under conditions of stress confinement results in the generation of high compressive stresses in the surface region of the target, Fig. 3.8a. The interaction of the initial compressive stresses with the free surface of the target results in the development of a tensile component of the pressure wave that propagates deeper into the bulk of the target. The tensile stresses are increasing with depth and can overcome the dynamic strength of the target material, leading to the mechanical separation and ejection of a front layer of the target, Fig. 3.8b. At later times, the layer ejected from the front surface can disintegrate into clusters/droplets, whereas the pressure wave can reach the back surface of the target and cause back-surface spallation, Fig. 3.8c.

As an example, the evolution of temperature and pressure in the surface region of an irradiated target leading to the spallation is shown in Fig. 3.9 for a TTM–MD simulation of a bulk Ni target irradiated by a 1 ps laser pulse [82, 109]. The rapid heating of the lattice due to the energy transfer from the excited electrons results in the build up of high compressive stresses in the surface region of the target. The relaxation of the compressive stresses leads to the generation of an unloading tensile wave that propagates from the surface of the target and increases its strength with depth. At a certain depth under the surface the tensile stresses exceed the dynamic strength of the melted metal, leading to the separation (spallation) of ∼25-nm-thick liquid layer from the target. The ability of the liquid to withstand the dynamic loading decreases with increasing temperature, shifting the depth of the laser-induced void nucleation and spallation closer to the surface and away from the depth at which the maximum tensile stresses are reached [68, 70, 82, 109].

The microscopic mechanisms of front-surface laser spallation have been investigated in a number of MD simulations performed for molecular systems [78–82, 164], metal targets [65, 68, 70, 76, 82, 109], and "generic" systems described by Lennard–Jones interatomic potential [75,77]. Nucleation, growth, and coalescence of voids have been identified as the main processes responsible for laser spallation. A visual picture of the spallation process is provided

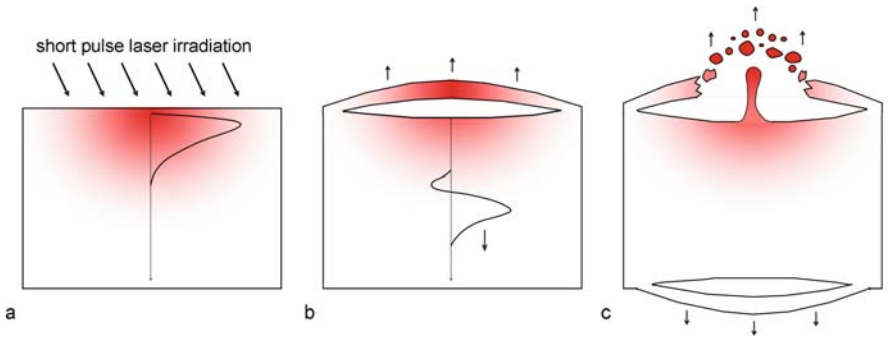

Fig. 3.8. Schematic representation of the processes involved in laser-induced front- and back-surface spallation: (**a**) generation of high compressive stresses in the surface region of the irradiated target; (**b**) propagation of the pressure wave deeper into the target, development of the tensile component of the pressure wave, separation and ejection of a front layer of the target (front-surface laser spallation) at a depth where the tensile component of the wave exceeds the dynamics strength of the (typically melted) material; (**c**) interaction of the pressure wave with the back surface of the target leading to the back-surface spallation, disintegration of the layer ejected from the front surface into clusters/droplets

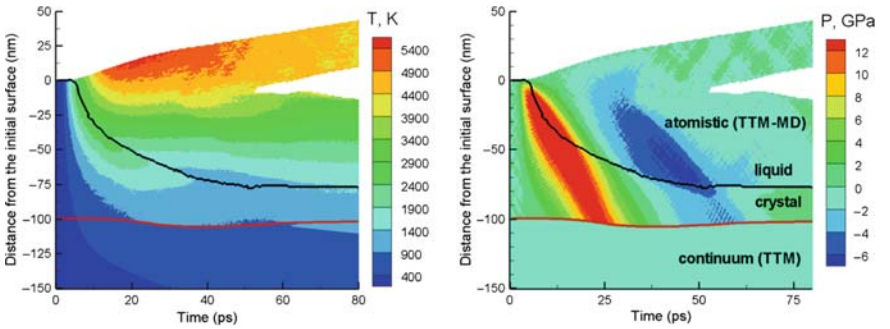

Fig. 3.9. Temperature and pressure contour plots in a simulation of a bulk Ni target irradiated with a 1 ps laser pulse at an absorbed fluence of 1935 J m^{-2}. Laser pulse is directed along the Y-axis, from the top of the contour plots. Black line separates the melted region from the crystalline bulk of the target. Red line separates the atomistic and continuum parts of the combined TTM–MD model. Areas where the density of the material is less than 10% of the initial density before the irradiation are not shown in the plots. The data are from [82, 109]

in the left part of Fig. 3.10, where the evolution of voids (empty space) is shown for a simulation performed for a 100 nm Ni film irradiated by a 1 ps laser pulse at an absorbed fluence of 1623 J m^{-2}. An active growth of voids starts at ∼32–35 ps, the time corresponding to the concentration of the tensile stresses associated with the interaction of the unloading stress wave, propagating from the irradiated surface, and the second tensile wave, generated

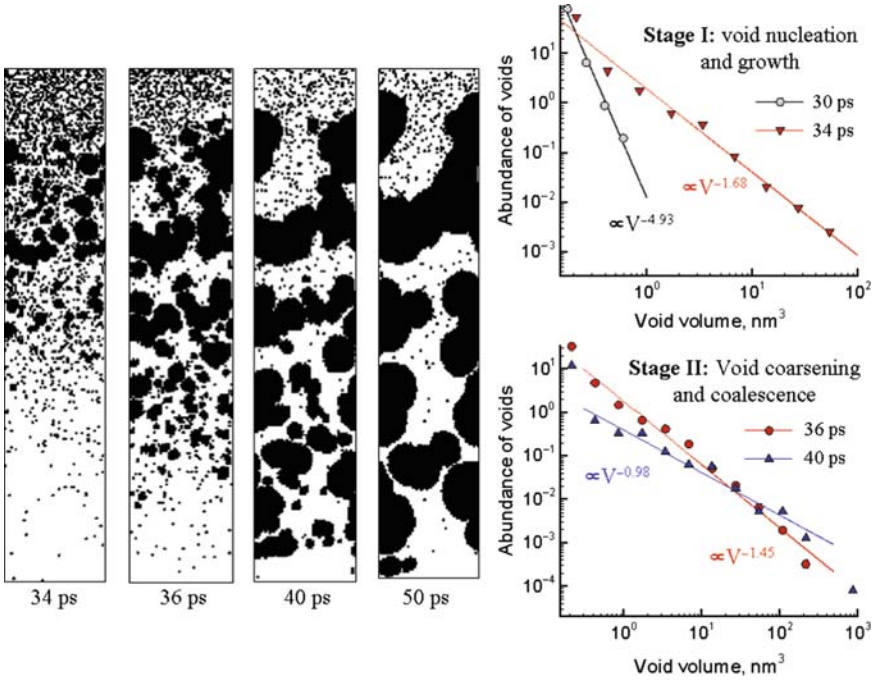

Fig. 3.10. Visual picture of the evolution of voids (empty space) in a sub-surface region of a 100 nm Ni film irradiated with a 1 ps laser pulse at an absorbed fluence of $1623\,\mathrm{J\,m^{-2}}$ and corresponding void abundance distributions. The laser pulse is directed from the top of the figure and the region shown in the snapshots is located ∼20 nm below the surface. The lines in the distributions are power law fits of the data points with the exponents indicated in the figures. The data are from [68]

upon the reflection of the original compressive wave from the back surface of the free-standing film [68, 82]. The area affected by the photomechanical damage quickly expands, and the size of the voids increases with time.

Quantitative information on the evolution of voids in the simulation discussed above is presented in the form of the void volume distributions in the right part of Fig. 3.10. All distributions can be relatively well described by a power law $N(V) \sim V^{-\tau}$, with an exponent $-\tau$ gradually increasing with time. Two distinct stages can be identified in the evolution of the void volume distributions. The initial stage of the *void nucleation and growth* is characterized by the increase in both the number of voids and the range of void sizes, as can be seen from the distributions shown for 30 and 34 ps after the laser pulse. The second stage of the evolution of the photomechanical damage corresponds to the *void coarsening and coalescence*, when the number of large voids increases at the expense of quickly decreasing population of small voids, e.g., compare the distributions for 36 and 40 ps. The second stage of the void evolution leads

to the eventual percolation of the empty volume and ejection of large liquid layer (or droplets) from the irradiated side of the film.

The two stages in the evolution of void volume distribution, discussed above for photomechanical spallation of a metal film [68], have also been observed in simulations of laser spallation of molecular targets [82]. Moreover, the time dependences of the power law exponent predicted in the simulations performed for these two drastically different materials, amorphous molecular systems [82] and crystalline metal targets [68, 82], are in an excellent quantitative agreement with each other. The power law dependences have also been reported for the void volume distributions observed in MD simulations of shock-induced, back-surface spallation of metal targets [165]. The critical power law exponent predicted for void distribution in the MD simulations of shock-induced, back-surface spallation, $\tau \sim 2.2$, is close to the ones that separate the two regimes of void evolution observed in the simulations of laser-induced, front-surface spallation of the molecular and metal targets [68, 82]. These observations suggest that the spallation mechanisms identified in [68,82] and briefly described in this section may reflect general characteristics of the dynamic fracture at high deformation rates.

3.3.4 Phase Explosion and Laser Ablation

At a sufficiently high laser fluence, the surface region of the irradiated target can be overheated above the limit of its thermodynamic stability, leading to an explosive decomposition of the overheated material into a mixture of vapor and liquid droplets. This process, commonly called "phase explosion" or "explosive boiling," results in the ejection (ablation) of a multicomponent plume consisting of individual atoms/molecules, small clusters, and larger liquid droplets.

The mechanisms of laser ablation have been extensively investigated in MD simulations addressing various aspects of the ablation process [70, 78, 79, 83–115]. One of the findings of the simulations is the existence of a well-defined threshold fluence for the transition from surface evaporation (desorption regime) to the collective material ejection (ablation regime) [70, 79, 100, 104, 109]. The threshold behavior in laser ablation can be related to the sharp transition from a metastable superheated liquid to a two-phase mixture of liquid and vapor (explosive boiling) at a temperature of approximately 90% of the critical temperature, as predicted based on the classical nucleation theory [166–169] and confirmed in simulations [170]. Experimental observations of the existence of a threshold fluence for the onset of the droplet ejection, as well as a steep increase of the ablation rate at the threshold, have also been interpreted as evidence of the transition from normal vaporization to the phase explosion [169, 171–173].

The active processes occurring in the vicinity of the irradiated surface during the first hundreds of picoseconds after the laser irradiation are illustrated in Fig. 3.11, where snapshots from a coarse-grained MD simulation of laser

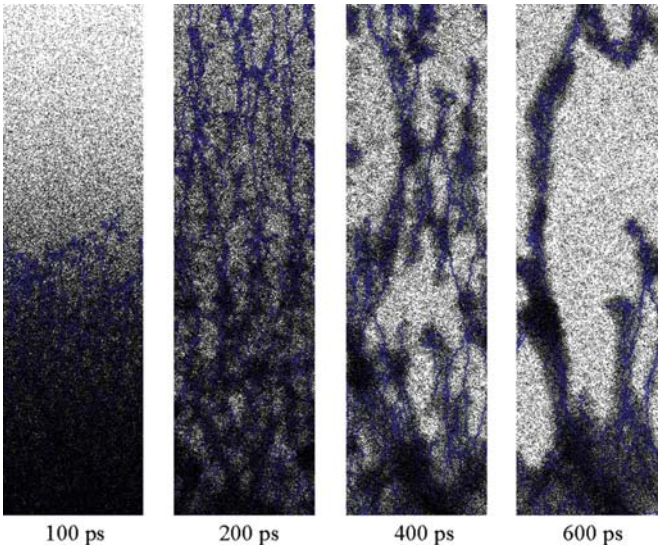

Fig. 3.11. Snapshots from a coarse-grained MD simulation of laser ablation of a polymer solution with polymer concentration of 6 wt.% [113]. The model is parameterized to represent PMMA in toluene and the simulation is performed at an absorbed laser fluence of 80 J m^{-2}, pulse duration of 50 ps, and optical penetration depth of 50 nm. Matrix molecules and units of polymer chains are shown by black and blue dots, respectively

ablation of a frozen polymer solution with polymer concentration of 6 wt.% are shown. The simulation is performed with a laser pulse duration of 50 ps, optical penetration depth of 50 nm, and an absorbed laser fluence of 80 J m^{-2}, about twice the ablation threshold for this model system [113]. In the first snapshot, shown for 100 ps, 50 ps after the end of the laser pulse, we see a homogeneous expansion of a significant part of the surface region. The homogeneous expansion is followed by the appearance of density fluctuations and gradual decomposition of the expanding plume into gas-phase molecules and liquid-phase regions. The decomposition of the expanding plume leads to the formation of a foamy transient structure of interconnected liquid regions, as shown in the snapshot at 200 ps. The foamy transient structure subsequently decomposes into separate liquid regions and vapor-phase molecules, forming a multicomponent ablation plume that expands away from the target.

While in the simulations performed for one-component molecular targets the liquid regions emerging from the explosive decomposition of the overheated region quickly develop into well-defined spherical liquid droplets [110,174], the entanglement of polymer chains in laser ablation of polymer solutions facilitates the formation of intricate, elongated viscous structures that extend far above the ablating surface, e.g., snapshot for 600 ps in Fig. 3.11. The elongated liquid structures that eventually separate from the target can be stabilized

by evaporative cooling in the expanding plume and can reach the substrate in matrix-assisted pulsed laser evaporation (MAPLE) film deposition technique [175–177], contributing to the roughness of the deposited films [178–182] (see Chap. 9 of this book for a detailed discussion of MAPLE). Indeed, the ejection of the extended liquid structures observed in the simulations [113], can be related to "nanofiber" or "necklace" polymer surface features observed in SEM images of PMMA films deposited in MAPLE [124–126,182], as well as in films fabricated by ablation of a polymer target involving a partial thermal decomposition of the target material into volatile species [183]. Moreover, the effect of dynamic molecular redistribution in the ejected matrix-polymer droplets, leading to the generation of transient "molecular balloons" in which polymer-rich surface layers enclose the volatile matrix material, has been identified in the simulations [114,126,184] as the mechanism responsible for the formation of characteristic wrinkled polymer structures observed experimentally in films deposited by MAPLE [114, 126, 182].

Regardless of the specific characteristics of the phase explosion affected by the properties of the target material and irradiation conditions, an important general conclusion that can be drawn from the results of MD simulations performed for different target materials, from metals to multicomponent molecular systems, is that particles/droplets and small atomic/molecular clusters are unavoidable products of the processes responsible for the material ejection in the ablation regime, e.g., [70, 87–89, 109, 110, 113, 125]. The energy density deposited by the laser pulse is decreasing with depth under the irradiated surface, leading to the strong dependence of the character of material decomposition from the depth of origin of the ejected material. Even when the laser fluence is sufficiently high to induce a complete vaporization of the surface layer of the target, the decrease of the energy density with depth results in the increase in the fraction of the liquid phase that emerges from the explosive phase decomposition [110, 185]. Since it is the amount of the released vapor phase that provides the driving force for the material decomposition and plume expansion, the decomposition process becomes less vigorous with depth, resulting in lower ejection velocities of droplets/clusters produced at higher depth in the target.

The difference in the characteristics of the phase explosion occurring in different parts of the target results in the effect of spatial segregation of clusters/droplets of different sizes in the plume. In particular, a detailed analysis of the dynamics of the plume formation in simulations performed for molecular targets with both long (no stress confinement) [110] and short (stress confinement) [185] laser pulses and fluences about twice the threshold for the ablation onset, reveals that only small clusters and monomers are ejected at the front of the expanding plume, medium-sized clusters are localized in the middle of the expanding plume, whereas the larger liquid droplets formed later during the plume development tend to be slower and are closer to the original surface. The cluster segregation effect, predicted in the simulations, can be related to the recent results of plume imaging experiments [186–190], where

splitting of the plume into a fast component with optical emission characteristic for neutral atoms and a slow component with blackbody-like emission attributed to the presence of hot clusters [191], is observed. Similarly, and consistently with the results of the simulations discussed in [110, 185], a layered structure of the plume (vaporized layer followed by small particles and larger droplets) observed in nanosecond laser ablation of water and soft tissue [192], is attributed to the succession of phase transitions occurring at different depths in the irradiated target [192, 193]. More examples of experimental observations suggesting the spatial segregation of clusters/droplets of different sizes in the plume can be found in Chap. 6 of this book.

Despite being ejected from deeper under the surface, where the energy density deposited by the laser pulse is smaller, the larger clusters in the plume are found to have substantially higher internal temperatures when compared with the smaller clusters [110, 185]. The lower temperature of the smaller clusters can be attributed to a more vigorous phase explosion (a larger fraction of the vapor-phase molecules is released due to a higher degree of overheating) and a fast expansion of the upper part of the plume that provides a more efficient cooling when compared with a slower cooling of the larger clusters dominated by evaporation.

Depending on the irradiation conditions, as well as the thermodynamic, mechanical, and electronic properties of the target material, the thermal phase explosion may be intertwined with other processes, such as the generation of the thermoelastic stresses in the regime of stress confinement (see Sect. 3.3.3), photochemical reactions in organic systems, or optical breakdown plasma generation in dielectrics. In particular, it has been observed in MD simulations of molecular systems [78, 79] and metals [109] that larger and more numerous clusters with higher ejection velocities are produced by the explosive phase decomposition in the regime of stress confinement when compared with simulations performed at the same laser fluences, but with longer pulses, in the regime of thermal confinement. Moreover, the transient tensile stresses generated in the regime of stress confinement can bring the system deeper into the metastable region and induce nucleation and growth of vapor bubbles at fluences at which no homogeneous boiling takes place without the assistance of thermoelastic stresses [5, 193, 194], thus shifting the threshold fluence for the ablation onset to lower values [78, 79, 109].

3.4 Concluding Remarks

MD simulation technique has successfully been adopted for simulation of laser–materials interactions. Recent developments of the coarse-grained models for molecular systems and a combined continuum-atomistic TTM–MD model for metals have provided computationally efficient means for incorporation of a description of the laser energy coupling and equilibration into

the classical MD method. The design of special heat-conductive, pressure-transmitting boundary conditions eliminates the need to model parts of the system where no structural transformations take place, further improving the efficiency of MD simulations of laser–materials interactions.

The examples of application of the MD simulation technique, briefly reviewed in this chapter, demonstrate the ability of atomic/molecular-level simulations to provide insights into the complex nonequilibrium processes responsible for material modification or removal in laser-processing applications. MD simulations of laser melting, generation of crystal defects, spallation, and ablation have already made contributions to the interpretation of experimental results and the advancement of theoretical understanding of laser-induced processes. With further innovative development of computational methodology and the fast growth of the available computing resources, one can expect that MD modeling will continue to play an increasingly important role in the investigation of laser interactions with materials.

One of the challenging directions of future work is the development of multiscale models for simulation of the processes occurring at the length-scale of the entire laser spot. For investigation of the long-term expansion of the ablation plume, in particular, a combination of MD with the DSMC method [195] has been demonstrated to be a promising approach capable of following the evolution of the parameters of the ablation plume on the scales, characteristic for experimental conditions, up to hundreds of microseconds and millimeters [50–55]. In the combined MD–DSMC model [78,185,187,196–199], MD is used for simulation of the initial stage of the ablation process (first nanoseconds) and provides the initial conditions for DSMC simulation of the processes occurring during the long-term expansion of the ejected plume. First applications of the combined MD–DSMC model for simulation of laser interactions with molecular systems have demonstrated the ability of the model to reveal interrelations between the processes occurring at different time- and length-scales and responsible for the evolution of the characteristics of the ablation plume [187, 197–199]. In particular, the initial generation of clusters in the phase explosion, predicted in MD simulations, is found to provide cluster precursors for condensation during the long-term plume expansion, thus eliminating the three-body collision bottleneck in the cluster growth process (see Chap. 5). The presence of clusters makes a strong impact on the following collisional condensation and evaporation processes, affecting the cluster composition of the plume, as well as the overall dynamics of the plume expansion [187, 197–199].

In addition to using MD model for direct simulation of laser–materials interactions, the detailed information on laser-induced structural and phase transformations, revealed in MD simulations, can help in the development of continuum-level hydrodynamic models. As briefly discussed in the introduction, the adaptation of the hydrodynamic computational models based on multiphase equations-of-state [56–62] for simulations of laser–materials interactions involve a number of assumptions on the kinetics of phase transformations,

evolution of photomechanical damage under the action of laser-induced tensile stresses, characteristics of the ablation plume generated as a result of the explosive decomposition of the overheated surface region in laser ablation, etc. The results of MD simulations on the kinetics and mechanisms of melting, spallation, and ablation, e.g., [66,68,82,109,110,152,170,200], can be used to provide the necessary information for the design of a reliable description of the fast nonequilibrium processes within a continuum model [60, 61, 96].

Further expansion of the domain of applicability of the MD-type of simulations into the area of laser interactions with complex multicomponent systems, such as nanocomposite materials or biological tissue, may involve the design of novel mesoscopic models, possibly based on the dynamic elements different from spherical particles, e.g., [201, 202]. Finally, an incorporation of the information on the transient changes in the interatomic bonding and thermophysical properties of the target material in the electronically excited state (Stages 1 and 2 in Fig. 3.1), revealed in electronic structure calculations and theoretical analysis, e.g., [23–36, 131–133], into large-scale atomistic simulations is needed for investigation of the implications of the initial ultrafast atomic dynamics for the final outcome of short-pulse laser irradiation.

Acknowledgements

Financial support of this work is provided by the National Science Foundation (USA) through grants CTS-0348503, DMII-0422632, CMMI-0800786, and DMR-0907247. The authors would like to thank Barbara J. Garrison of Penn State University (USA), Aaron T. Sellinger and James M. Fitz-Gerald of the University of Virginia (USA), Antonio Miotello of the University of Trento (Italy), Nadezhda Bulgakova of the Institute of Thermophysics SB RAS (Russia), Alfred Vogel of the Institute of Biomedical Optics in Lübeck (Germany), Roland Hergenröder of the Institute for Analytical Sciences in Dortmund (Germany), and Tatiana Itina and Jörg Hermann of the CNRS Laboratory of Lasers, Plasmas, and Photonic Processing in Marseille (France), for insightful and stimulating discussions.

References

1. D. Bäuerle, *Laser Processing and Chemistry* (Springer, Berlin, 2000)
2. R.R. Gattass, E. Mazur, Nat. Photon. **2**, 219–225 (2008)
3. D.B. Chrisey, G.K. Hubler (eds), *Pulsed Laser Deposition of Thin Films* (Wiley, New York, 1994)
4. M.H. Niemz, *Laser-Tissue Interactions: Fundamentals and Applications* (Springer, Berlin, 1996)
5. A. Vogel, V. Venugopalan, Chem. Rev. **103**, 577–644 (2003)
6. V. Zafiropulos, in *Laser Cleaning*, ed. by B. Luk'yanchuk (World Scientific, Singapore, 2002), p. 343
7. A. Nevin, P. Pouli, S. Georgiou, C. Fotakis, Nat. Mater. **6**, 320–322 (2007)

8. E.I. Moses, R.E. Bonanno, C.A. Haynam, R.L. Kauffman, B.J. MacGowan, R.W. Patterson Jr, R.H. Sawicki, B.M. Van Wonterghem, Eur. Phys. J. D **44**, 215–218 (2007)
9. L. Huang, J.P. Callan, E.N. Glezer, E. Mazur, Phys. Rev. Lett. **80**, 185–188 (1998)
10. M.B. Agranat, S.I. Ashitkov, V.E. Fortov, A.V. Kirillin, A.V. Kostanovskii, S.I. Anisimov, P.S. Kondratenko, Appl. Phys. A 69, 637–640 (1999)
11. C. Guo, G. Rodriguez, A. Lobad, A.J. Taylor, Phys. Rev. Lett. **84**, 4493–4496 (2000)
12. O.P. Uteza, E.G. Gamaly, A.V. Rode, M. Samoc, B. Luther-Davies, Phys. Rev. B **70**, 054108 (2004)
13. J. Wang, C. Guo, Phys. Rev. B **75**, 184304 (2007)
14. A. Rousse, G. Rischel, S. Fourneaux, I. Uschmann, S. Sebban, G. Grillon, P.h. Balcou, E. Förster, J.P. Geindre, P. Audebert, J.C. Gauthier, D. Hulin, Nature **410**, 65–68 (2001)
15. A.M. Lindenberg, J. Larsson, K. Sokolowski-Tinten, K.J. Gaffney, C. Blome, O. Synnergren, J. Sheppard, C. Caleman, A.G. MacPhee, D. Weinstein, D.P. Lowney, T.K. Allison, T. Matthews, R.W. Falcone, A.L. Cavalieri, D.M. Fritz, S.H. Lee, P.H. Bucksbaum, D.A. Reis, J. Rudati, P.H. Fuoss, C.C. Kao, D.P. Siddons, R. Pahl, J. Als-Nielsen, S. Duesterer, R. Ischebeck, H. Schlarb, H. Schulte-Schrepping, T.H. Tschentscher, J. Schneider, D. von der Linde, O. Hignette, F. Sette, H.N. Chapman, R.W. Lee, T.N. Hansen, S. Techert, J.S. Wark, M. Bergh, G. Huldt, D. van der Spoel, N. Timneanu, J. Hajdu, R.A. Akre, E. Bong, P. Krejcik, J. Arthur, S. Brennan, K. Luening, J.B. Hastings, Science **308**, 392–395 (2005)
16. K. Sokolowski-Tinten, C. Blome, J. Blums, A. Cavalleri, C. Dietrich, A. Tarasevich, I. Uschmann, E. Förster, M. Kammler, M. Horn-von-Hoegen, D. von der Linde, Nature **422**, 287–289 (2003)
17. W.E. King, G.H. Campbell, A. Frank, B. Reed, J.F. Schmerge, B.J. Siwick, B.C. Stuart, P.M. Weber, J. Appl. Phys. **97**, 111101 (2005)
18. S. Williamson, G. Mourou, J.C.M. Li, Phys. Rev. Lett. **52**, 2364–2367 (1984)
19. B.J. Siwick, J.R. Dwyer, R.E. Jordan, R.J.D. Miller, Science **302**, 1382–1385 (2003)
20. J.R. Dwyer, R.E. Jordan, C.T. Hebeisen, M. Harb, R. Ernstorfer, T. Dartigalongue, R.J.D. Miller, J. Mod. Optics **54**, 905–922 (2007)
21. M. Harbst, T.N. Hansen, C. Caleman, W.K. Fullagar, P. Jönsson, P. Sondhauss, O. Synnergren, J. Larsson, Appl. Phys. A **81**, 893–900 (2005)
22. A.M. Lindenberg, S. Engemann, K.J. Gaffney, K. Sokolowski-Tinten, J. Larsson, P.B. Hillyard, D.A. Reis, D.M. Fritz, J. Arthur, R.A. Akre, M.J. George, A. Deb, P.H. Bucksbaum, J. Hajdu, D.A. Meyer, M. Nicoul, C. Blome, T.H. Tschentscher, A.L. Cavalieri, R.W. Falcone, S.H. Lee, R. Pahl, J. Rudati, P.H. Fuoss, A.J. Nelson, P. Krejcik, D.P. Siddons, P. Lorazo, J.B. Hastings, Phys. Rev. Lett. **100**, 135502 (2008)
23. S. Mazevet, J. Clérouin, V. Recoules, P.M. Anglade, G. Zerah, Phys. Rev. Lett. **95**, 085002 (2005)
24. V. Recoules, J. Clérouin, G. Zérah, P.M. Anglade, S. Mazevet, Phys. Rev. Lett. **96**, 055503 (2006)
25. F. Bottin, G. Zérah, Phys. Rev. B **75**, 174114 (2007)
26. D. Dundas, J. Phys. B: At. Mol. Opt. Phys. **37**, 2883–2901 (2004)

27. H.O. Jeschke, M.E. Garcia, Chap. 7 in *Nonlinear Optics, Quantum Optics, and Ultrafast Phenomena with X-Rays,* ed. by B.W. Adams (Springer, New York, 2003), p. 175
28. H.O. Jeschke, M.E. Garcia, M. Lenzner, J. Bonse, J. Krüger, W. Kautek, Appl. Surf. Sci. **197/198**, 839–844 (2002)
29. P.L. Silvestrelli, A. Alavi, M. Parrinello, D. Frenkel, Phys. Rev. Lett. **77**, 3149–3152 (1996)
30. P.L. Silvestrelli, Phys. Rev. B **60**, 16382–16388 (1999)
31. P.L. Silvestrelli, A. Alavi, M. Parrinello, D. Frenkel, Phys. Rev. B **56**, 3806–3812 (1997)
32. L.X. Benedict, C.D. Spataru, S.G. Louie, Phys. Rev. B **66**, 085116 (2002)
33. P.B. Hillyard, D.A. Reis, K.J. Gaffney, Phys. Rev. B **77**, 195213 (2008)
34. R.E. Allen, T. Dumitrica, B. Torralva, Chap. 7 in *Ultrafast Physical Processes in Semiconductors,* ed. by K.T. Tsen (Academic, New York, 2000), p. 315
35. B. Torralva, T.A. Niehaus, M. Elstner, S. Suhai, T.h. Frauenheim, R.E. Allen, Phys. Rev. B **64**, 153105 (2001)
36. T. Dumitrica, A. Burzo, Y. Dou, R.E. Allen, Phys. Stat. Solidi B **241**, 2331–2342 (2004)
37. V.A. Gnatyuk, T. Aoki, O.S. Gorodnychenko, Y. Hatanaka, Appl. Phys. Lett. **83**, 3704–3706 (2003)
38. K.N. Vonatsos, D.I. Pantelis, Appl. Phys. A **80**, 885–889 (2005)
39. V.N. Tokarev, A.F.H. Kaplan, J. Appl. Phys. **86**, 2836–2846 (1999)
40. R.Černý R. Šáršik, I. Lukeš, V. Cháb, Phys. Rev. B **44**, 4097–4102 (1991)
41. X. Xu, G. Chen, K.H. Song, Int. J. Heat Mass Transf. **42**, 1371–1382 (1999)
42. J.C. Kapat, Z. Wei, A. Kumar, Appl. Surf. Sci. **127–129**, 212–217 (1998)
43. G.X. Wang, E.F. Matthys, Trans. ASME **118**, 944–951 (1996)
44. I.H. Chowdhury, X. Xu, Num. Heat Transf. A **44**, 219–232 (2003)
45. R.K. Singh, J. Narayan, Phys. Rev. B **41**, 8843–8858 (1990)
46. A. Peterlongo, A. Miotello, R. Kelly, Phys. Rev. E **50**, 4716–4727 (1994)
47. J.R. Ho, C.P. Grigoropoulos, J.A.C. Humphrey, J. Appl. Phys. **78**, 4696–4709 (1995)
48. A. Bogaerts, Z. Chen, R. Gijbels, A. Vertes, Spectrochim. Acta. B **58**, 1867–1893 (2003)
49. Z. Chen, A. Vertes, Phys. Rev. E **77**, 036316 (2008)
50. I. NoorBatcha, R.R. Lucchese, Y. Zeiri, J. Chem. Phys. **86**, 5816–5824 (1987)
51. H.M. Urbassek, D. Sibold, Phys. Rev. Lett. **70**, 1886–1889 (1993)
52. O. Ellegaard, J. Schou, H.M. Urbassek, Appl. Phys. A **69**, S577-S582 (1999)
53. T.E. Itina, W. Marine, M. Autric, J. Appl. Phys. **82**, 3536–3542 (1997)
54. T.E. Itina, W. Marine, M. Autric, J. Appl. Phys. **85**, 7905–7908 (1999)
55. A.A. Morozov, Phys. Fluids **19**, 087101 (2007)
56. K. Eidmann, J. Meyer-ter-Vehn, T. Schlegel, S. Huller, Phys. Rev. E **62**, 1202–1214 (2000)
57. Y. Kondoh, T. Yabe, J. Maehara, T. Nakamura, Y. Ogata, Phys. Rev. E **68**, 066408 (2003)
58. F. Vidal, T.W. Johnston, J.C. Kieffer, F. Martin, Phys. Rev. B **70**, 184125 (2004)
59. J.P. Colombier, P. Combis, F. Bonneau, R. Le Harzic, E. Audouard, Phys. Rev. B **71**, 165406 (2005)
60. M.E. Povarnitsyn, T.E. Itina, M. Sentis, K.V. Khishchenko, P.R. Levashov, Phys. Rev. B **75**, 235414 (2007)

61. A.N. Volkov, L.V. Zhigilei, J. Phys. Conf. Ser. **59**, 640–645 (2007)
62. A.N. Volkov, C. Sevilla, L.V. Zhigilei, Appl. Surf. Sci. **253**, 6394–6399 (2007)
63. C.F. Richardson, P. Clancy, Mol. Simul. **7**, 335–355 (1991)
64. H. Hakkinen, U. Landman, Phys. Rev. Lett. **71**, 1023–1026 (1993)
65. D.S. Ivanov, L.V. Zhigilei, Phys. Rev. B **68**, 064114 (2003)
66. D.S. Ivanov, L.V. Zhigilei, Phys. Rev. Lett. **91**, 105701 (2003)
67. D.S. Ivanov, L.V. Zhigilei, Appl. Phys. A **79**, 977–981 (2004)
68. L.V. Zhigilei, D.S. Ivanov, E. Leveugle, B. Sadigh, E.M. Bringa, in *High-Power Laser Ablation V*, ed. by C.R. Phipps, Proc. SPIE **5448**, 505–519 (2004)
69. L.V. Zhigilei, D.S. Ivanov, Appl. Surf. Sci. **248**, 433–439 (2005)
70. L.V. Zhigilei, Z. Lin, D.S. Ivanov, in *Proceedings of the 2006 ASME International Mechanical Engineering Congress and Exposition (IMECE2006)*, ASME paper IMECE2006–16305 (2006)
71. Z. Lin, L.V. Zhigilei, Phys. Rev. B **73**, 184113 (2006)
72. Z. Lin, L.V. Zhigilei, J. Phys. Conf. Ser. **59**, 11–15 (2007)
73. W.H. Duff, L.V. Zhigilei, J. Phys. Conf. Ser. **59**, 413–417 (2007)
74. Z. Lin, R.A. Johnson, L.V. Zhigilei, Phys. Rev. B **77**, 214108 (2008)
75. S.I. Anisimov, V.V. Zhakhovskii, N.A. Inogamov, K. Nishihara, A.M. Oparin, Y.V. Petrov, Pis'ma Zh. Eksp. Teor. Fiz. **77**, 731–736 (2003) [JETP Lett. **77**, 606–610 (2003)]
76. A.K. Upadhyay, H.M. Urbassek, J. Phys. D **38**, 2933–2941 (2005)
77. H.Y. Lai, P.H. Huang, Appl. Surf. Sci. **254**, 3067–3073 (2008)
78. L.V. Zhigilei, E. Leveugle, B.J. Garrison, Y.G. Yingling, M.I. Zeifman, Chem. Rev. **103**, 321–348 (2003)
79. L.V. Zhigilei, B.J. Garrison, J. Appl. Phys. **88**, 1281–1298 (2000)
80. A.G. Zhidkov, L.V. Zhigilei, A. Sasaki, T. Tajima, Appl. Phys. A **73**, 741–747 (2001)
81. E. Leveugle, L.V. Zhigilei, Appl. Phys. A **79**, 753–756 (2004)
82. E. Leveugle, D.S. Ivanov, L.V. Zhigilei, Appl. Phys. A **79**, 1643–1655 (2004)
83. E. Ohmura, I. Fukumoto, Int. J. Japan Soc. Prec. Eng. **30**, 128–133 (1996)
84. E. Ohmura, I. Fukumoto, I. Miyamoto, Int. J. Jpn. Soc. Precis. Eng. **32**, 248–253 (1998)
85. R.F.W. Herrmann, J. Gerlach, E.E.B. Campbell, Appl. Phys. A **66**, 35–42 (1998)
86. X. Wu, M. Sadeghi, A. Vertes, J. Phys. Chem. B **102**, 4770–4778 (1998)
87. S. Kristyan, A. Bensura, A. Vertes, Theor. Chem. Acc. **107**, 319–325 (2002)
88. X. Xu, C. Cheng, I.H. Chowdhury, ASME Trans. J. Heat Transf. **126**, 727–734 (2004)
89. C. Cheng, X. Xu, Phys. Rev. B **72**, 165415 (2005)
90. X.W. Wang, X.F. Xu, J. Heat Transf. **124**, 265–274 (2002)
91. X.W. Wang, J. Phys. D **38**, 1805–1823 (2005)
92. P. Lorazo, L.J. Lewis, M. Meunier, Phys. Rev. B **73**, 134108 (2006)
93. P. Lorazo, L.J. Lewis, M. Meunier, Phys. Rev. Lett. **91**, 225502 (2003)
94. N.N. Nedialkov, P.A. Atanasov, Appl. Surf. Sci. **252**, 4411–4415 (2006)
95. N.N. Nedialkov, P.A. Atanasov, S.E. Imamova, A. Ruf, P. Berger, F. Dausinger, Appl. Phys. A **79**, 1121–1125 (2004)
96. S.I. Anisimov, V.V. Zhakhovskii, N.A. Inogamov, K. Nishihara, Y.V. Petrov, V.A. Khokhlov, J. Exp. Theor. Phys. **103**, 183–197 (2006)

97. M.B. Agranat, S.I. Anisimov, S.I. Ashitkov, V.V. Zhakhovskii, N.A. Inogamov, K. Nishihara, Y.V. Petrov, V.E. Fortov, V.A. Khokhlov, Appl. Surf. Sci. **253**, 6276–6282 (2007)
98. L.V. Zhigilei, P.B.S. Kodali, B.J. Garrison, J. Phys. Chem. B **101**, 2028–2037 (1997)
99. L.V. Zhigilei, B.J. Garrison, Appl. Phys. Lett. **71**, 551–553 (1997)
100. L.V. Zhigilei, P.B.S. Kodali, B.J. Garrison, Chem. Phys. Lett. **276**, 269–273 (1997)
101. L.V. Zhigilei, P.B.S. Kodali, B.J. Garrison, J. Phys. Chem. B **102**, 2845–2853 (1998)
102. L.V. Zhigilei, B.J. Garrison, Rapid Commun. Mass Spectrom. **12**, 1273–1277 (1998)
103. L.V. Zhigilei, B.J. Garrison, Appl. Phys. Lett. **74**, 1341–1343 (1999)
104. L.V. Zhigilei, B.J. Garrison, Appl. Phys. A **69**, S75–S80 (1999)
105. Y.G. Yingling, L.V. Zhigilei, B.J. Garrison, A. Koubenakis, J. Labrakis, S. Georgiou, Appl. Phys. Lett. **78**, 1631–1633 (2001)
106. Y.G. Yingling, L.V. Zhigilei, B.J. Garrison, J. Photochem. Photobiol. A **145**, 173–181 (2001)
107. T.E. Itina, L.V. Zhigilei, B.J. Garrison, J. Phys. Chem. B **106**, 303–310 (2002)
108. C. Schäfer, H.M. Urbassek, L.V. Zhigilei, Phys. Rev. B **66**, 115404 (2002)
109. L.V. Zhigilei, Z. Lin, D.S. Ivanov, J. Phys. Chem. C **113**, 11892–11906 (2009)
110. L.V. Zhigilei, Appl. Phys. A **76**, 339–350 (2003)
111. Y.G. Yingling, B.J. Garrison, J. Phys. Chem. B **109**, 16482–16489 (2005)
112. R. Knochenmuss, L.V. Zhigilei, J. Phys. Chem. B **109**, 22947–22957 (2005)
113. E. Leveugle, L.V. Zhigilei, J. Appl. Phys. **102**, 074914 (2007)
114. E. Leveugle, A. Sellinger, J.M. Fitz-Gerald, L.V. Zhigilei, Phys. Rev. Lett. **98**, 216101 (2007)
115. M. Prasad, P. Conforti, B.J. Garrison, J. Appl. Phys. **101**, 103113 (2007)
116. M.P. Allen, D.J. Tildesley, *Computer Simulation of Liquids* (Clarendon, Oxford, 1990, 1987)
117. D. Frenkel, B. Smit, *Understanding Molecular Simulation: From Algorithms to Applications* (Academic, San Diego, 1996)
118. K. Kadau, T.C. Germann, P.S. Lomdahl, Int. J. Mod. Phys. C **17**, 1755–1761 (2006)
119. http://folding.stanford.edu/
120. J.C. Deàk, L.K. Iwaki, S.T. Rhea, D.D. Dlott, J. Raman Spectrosc. **31**, 263–274 (2000)
121. S. Woutersen, H.J. Bakker, Nature **402**, 507–509 (1999)
122. H. Kim, D.D. Dlott, Y. Won, J. Chem. Phys. **102**, 5480–5485 (1995)
123. R.E. Wyatt, C. Iung, C. Leforestier, Acc. Chem. Res. **28**, 423–429 (1995)
124. E. Leveugle, L.V. Zhigilei, A. Sellinger, J.M. Fitz-Gerald, J. Phys. Conf. Ser. **59**, 126–131 (2007)
125. E. Leveugle, L.V. Zhigilei, A. Sellinger, J.M. Fitz-Gerald, Appl. Surf. Sci. **253**, 6456–6460 (2007)
126. A. Sellinger, E. Leveugle, J.M. Fitz-Gerald, L.V. Zhigilei, Appl. Phys. A **92**, 821 (2008)
127. E.A. Colbourn (ed.) *Computer Simulation of Polymers* (Longman Scientific and Technical, Harlow, 1994)
128. F. Gao, D.J. Bacon, P.E.J. Flewitt, T.A. Lewis, Modelling Simul. Mater. Sci. Eng. **6**, 543–556 (1998)

129. D.M. Duffy, A.M. Rutherford, J. Phys: Condens. Matter **19**, 016207 (2007)
130. S.I. Anisimov, B.L. Kapeliovich, T.L. Perel'man, Sov. Phys. JETP **39**, 375–377 (1974)
131. Z. Lin, L.V. Zhigilei, Appl. Surf. Sci. **253**, 6295–6300 (2007)
132. Z. Lin, L.V. Zhigilei, in *High-Power Laser Ablation VI*, ed. by C.R. Phipps, Proc. SPIE **6261**, 62610U (2006)
133. Z. Lin, L.V. Zhigilei, V. Celli, Phys. Rev. B **77**, 075133 (2008)
134. http://www.faculty.virginia.edu/CompMat/electron-phonon-coupling/
135. N. Rotenberg, A.D. Bristow, M. Pfeiffer, M. Betz, H.M. van Driel, Phys. Rev. B **75**, 155426 (2007)
136. M.S. Daw, S.M. Foiles, M.I. Baskes, Mater. Sci. Rep. **9**, 251–310 (1993)
137. S.M. Foiles, MRS Bull. **21**, 24–28 (1996)
138. X.W. Zhou, H.N.G. Wadley, R.A. Johnson, D.J. Larson, N. Tabat, A. Cerezo, A.K. Petford-Long, G.D.W. Smith, P.H. Clifton, R.L. Martens, T.F. Kelly, Acta Mater. **49**, 4005–4015 (2001)
139. D.S. Ivanov, B. Rethfeld, G.M. O'Connor, T.h.J. Glynn, A.N. Volkov, L.V. Zhigilei, Appl. Phys. A **92**, 791–796 (2008)
140. L.V. Zhigilei, B.J. Garrison, Mat. Res. Soc. Symp. Proc. **538**, 491–496 (1999)
141. C. Schafer, H.M. Urbassek, L.V. Zhigilei, B.J. Garrison, Comp. Mater. Sci. **24**, 421–429 (2002)
142. L.V. Zhigilei, B.J. Garrison, in *Laser-Tissue Interaction IX*, ed. by S.L. Jacques, Proc. SPIE **3254**, 135–143 (1998)
143. V. Vitek, Philos. Mag. **21**, 1275–1278 (1970)
144. J.P. Hirth, J. Lothe, *Theory of Dislocations*, 2nd edn. (Wiley, New York, 1982)
145. D. Ashkenasi, M. Lorenz, R. Stoian, A. Rosenfeld, Appl. Surf. Sci. **150**, 101–106 (1999)
146. P.T. Mannion, J. Magee, E. Coyne, G.M. O'Connor, T.J. Glynn, Appl. Surf. Sci. **233**, 275–287 (2004)
147. S.E. Kirkwood, A.C. van Popta, Y.Y. Tsui, R. Fedosejevs, Appl. Phys. A **81**, 729–735 (2005)
148. J. Krüger, D. Dufft, R. Koter, A. Hertwig, Appl. Surf. Sci. **253**, 7815–7819 (2007)
149. G. Raciukaitis, M. Brikas, P. Gecys, M. Gedvilas, Proc. SPIE **7005**, 70052L (2008)
150. J.G. Dash, Rev. Mod. Phys. **71**, 1737–1743 (1999)
151. P.R. Couchman, W.A. Jesser, Nature **269**, 481–483 (1977)
152. D.S. Ivanov, L.V. Zhigilei, Phys. Rev. Lett. **98**, 195701 (2007)
153. B. Rethfeld, K. Sokolowski-Tinten, D. von der Linde, S.I. Anisimov, Phys. Rev. B **65**, 092103 (2002)
154. J.R. Dwyer, C.T. Hebeisen, R. Ernstorfer, M. Harb, V. Deyirmenjian, R.E. Jordan, R.J.D. Miller, Phil. Trans. R. Soc. A **364**, 741–778 (2006)
155. S.N. Luo, T.J. Ahrens, T. Çağın, A. Strachan, W.A. Goddard, D.C. Swift, Phys. Rev. B **68**, 134206 (2003)
156. V. Sorkin, E. Polturak, J. Adler, Phys. Rev. B **68**, 174102 (2003)
157. G. Paltauf, P.E. Dyer, Chem. Rev. **103**, 487–518 (2003)
158. I. Itzkan, D. Albagli, M.L. Dark, L.T. Perelman, C. von Rosenberg, M.S. Feld, Proc. Natl. Acad. Sci. U S A **92**, 1960–1964 (1995)
159. A.A. Oraevsky, S.L. Jacques, F.K. Tittel, J. Appl. Phys. **78**, 1281–1290 (1995)
160. R. Cramer, R.F. Haglund Jr., F. Hillenkamp, Int. J. Mass Spectrom. Ion Proc. **169/170**, 51–67 (1997)

161. H. Tamura, T. Kohama, K. Kondo, M. Yoshida, J. Appl. Phys. **89**, 3520–3522 (2001)
162. V.E. Fortov, V.V. Kostin, S. Eliezer, J. Appl. Phys. **70**, 4524–4531 (1991)
163. G.I. Kanel', V.E. Fortov, S.V. Razorenov, Physics-Uspekhi **50**, 771–791 (2007)
164. Animated sequences of snapshots from a molecular dynamics simulation of laser spallation of a molecular target can be found at http://www.faculty.virginia.edu/CompMat/spallation/animations/
165. A. Strachan, T. Cagin, W.A. Goddard III, Phys. Rev. B **63**, 060103 (2001)
166. M.M. Martynyuk, Sov. Phys. Tech. Phys. **21**, 430–433 (1976)
167. A. Miotello, R. Kelly, Appl. Phys. A **69**, S67–S73 (1999)
168. R. Kelly, A. Miotello, J. Appl. Phys. **87**, 3177–3179 (2000)
169. N.M. Bulgakova, A.V. Bulgakov, Appl. Phys. A **73**, 199–208 (2001)
170. B.J. Garrison, T.E. Itina, L.V. Zhigilei, Phys. Rev. E **68**, 041501 (2003)
171. K.H. Song, X. Xu, Appl. Surf. Sci. **127–129**, 111–116 (1998)
172. J.H. Yoo, S.H. Jeong, X.L. Mao, R. Greif, R.E. Russo, Appl. Phys. Lett. **76**, 783–785 (2000)
173. C. Porneala, D.A. Willis, Appl. Phys. Lett. **89**, 211121 (2006)
174. Animated sequences of snapshots from a molecular dynamics simulation of laser ablation of a molecular target can be found at http://www.faculty.virginia.edu/CompMat/ablation/animations/
175. A. Piqué, R.A. McGill, D.B. Chrisey, J. Callahan, T.E. Mlsna, Mater. Res. Soc. Symp. Proc. **526**, 375–383 (1998)
176. A. Piqué, R.A. McGill, D.B. Chrisey, D. Leonhardt, T.E. Mslna, B.J. Spargo, J.H. Callahan, R.W. Vachet, R. Chung, M.A. Bucaro, Thin Solid Films **355/356**, 536–541 (1999)
177. D.B. Chrisey, A. Piqué, R.A. McGill, J.S. Horwitz, B.R. Ringeisen, D.M. Bubb, P.K. Wu, Chem. Rev. **103**, 553–576 (2003)
178. R. Fryček, M. Jelínek, T. Kocourek, P. Fitl, M. Vrňata, V. Myslík, M. Vrbová, Thin Solid Films **495**, 308–311 (2006)
179. D.M. Bubb, P.K. Wu, J.S. Horwitz, J.H. Callahan, M. Galicia, A. Vertes, R.A. McGill, E.J. Houser, B.R. Ringeisen, D.B. Chrisey, J. Appl. Phys. **91**, 2055–2058 (2002)
180. K. Rodrigo, P. Czuba, B. Toftmann, J. Schou, R. Pedrys, Appl. Surf. Sci. **252**, 4824–4828 (2006)
181. A. Gutierrez-Llorente, R. Perez-Casero, B. Pajot, J. Roussel, R.M. Defourneau, D. Defourneau, J.L. Fave, E. Millon, J. Perriere, Appl. Phys. A **77**, 785–788 (2003)
182. A.T. Sellinger, E.M. Leveugle, K. Gogick, L.V. Zhigilei, J.M. Fitz-Gerald, J. Vac. Sci. Technol. A **24**, 1618–1622 (2006)
183. J. Blazevska-Gilev et al., Polym. Degrad. Stab. **91**, 213–220 (2006)
184. Animated sequences of snapshots from a molecular dynamics simulation of the generation of "molecular balloons" in laser-induced explosive boiling of polymer solutions can be found at http://www.faculty.virginia.edu/CompMat/molecular-balloons/
185. L.V. Zhigilei, in *Advances in Materials Theory and Modeling-Bridging Over Multiple-Length and Time Scales*, ed. by V.V. Bulatov, F. Cleri, L. Colombo, L.J. Lewis, N. Mousseau, Mater. Res. Soc. Symp. Proc. **677** AA2.1.1 (2001)
186. S. Noël, J. Hermann, T. Itina, Appl. Surf. Sci. **253**, 6310–6315 (2007)
187. T.E. Itina, K. Gouriet, L.V. Zhigilei, S. Noël, J. Hermann, M. Sentis, Appl. Surf. Sci. **253**, 7656–7661 (2007)

188. S. Amoruso, R. Bruzzese, C. Pagano, X. Wang, Appl. Phys. A **89**, 1017–1024 (2007)
189. O. Albert, S. Roger, Y. Glinec, J.C. Loulergue, J. Etchepare, C. Boulmer-Leborgne, J. Perriere, E. Millon, Appl. Phys. A **76**, 319–323 (2003)
190. N. Jegenyes, J. Etchepare, B. Reynier, D. Scuderi, A. Dos-Santos, Z. Tóth, Appl. Phys. A **91**, 385–392 (2008)
191. D. Scuderi, R. Benzerga, O. Albert, B. Reynier, J. Etchepare, Appl. Surf. Sci. **252**, 4360–4363 (2006)
192. I. Apitz, A. Vogel, Appl. Phys. A **81**, 329–338 (2005)
193. A. Vogel, I. Apitz, V. Venugopalan, in *Oscillations, Waves and Interactions*, ed. by T. Kurz, U. Parlitz, U. Kaatze (Universitätsverlag Göttingen, Göttingen, 2007), p. 217
194. D. Kim, M. Ye, C.P. Grigoropoulos, Appl. Phys. A **67**, 169–181 (1998)
195. G.A. Bird, *Molecular Gas Dynamics and the Direct Simulation of Gas Flows* (Clarendon, Oxford, 1994)
196. L.V. Zhigilei, A.M. Dongare, Comput. Model. Eng. Sci **3**, 539–555 (2002)
197. M.I. Zeifman, B.J. Garrison, L.V. Zhigilei, J. Appl. Phys. **92**, 2181–2193 (2002)
198. M.I. Zeifman, B.J. Garrison, L.V. Zhigilei, Appl. Surf. Sci. **197/198**, 27–34 (2002)
199. T.E. Itina, L.V. Zhigilei, J. Phys. Conf. Ser **59**, 44–49 (2007)
200. T.E. Itina, Chem. Phys. Lett. **452**, 129–132 (2008)
201. L.V. Zhigilei, C. Wei, D. Srivastava, Phys. Rev. B **71**, 165417 (2005)
202. A.N. Volkov, K.R. Simov, L.V. Zhigilei, in *Proceedings of ASME International Mechanical Engineering Congress and Exposition*, ASME paper IMECE2008–68021 (2008)